University of Kentucky

UKnowledge

University of Kentucky Master's Theses   Graduate School

2011

INFLUENCE OF TISSUE ABSORPTION AND SCATTERING ON DIFFUSE CORRELATION SPECTROSCOPY BLOOD FLOW MEASUREMENTS

Daniel Irwin
University of Kentucky, daniel.irwin@uky.edu

Right click to open a feedback form in a new tab to let us know how this document benefits you.

Recommended Citation

ABSTRACT OF THESIS

INFLUENCE OF TISSUE ABSORPTION AND SCATTERING ON
DIFFUSE CORRELATION SPECTROSCOPY BLOOD FLOW MEASUREMENTS

This investigation evaluates the influences of optical property assumptions on near-infrared diffuse correlation spectroscopy (DCS) flow index measurements. Independent variation is induced in optical properties, absorption coefficient (μ_a) and reduced scattering coefficient (μ_s'), of liquid phantoms with concurrent measurements of flow indices. A hybrid instrument is incorporated consisting of a dual-wavelength (785 and 830 nm) DCS flow device to obtain flow indices and a frequency-domain tissue-oximeter for optical properties. Flow indices are calculated with measured μ_a and μ_s' or assumed constant μ_a and μ_s'. Inaccurate μ_s' assumptions produced much larger flow index errors than inaccurate μ_a. Underestimated/overestimated μ_s' from -35%/+175% lead to flow index errors of +110%/-80% and underestimated/overestimated μ_a from -40%/+150% lead to -20%/+40%, regardless of wavelength. Analysis of a clinical study involving human head and neck tumors indicates flow index errors due to inter-patient optical property variations up to +280%. Collectively, these findings suggest that studies involving significant μ_a and μ_s' changes should measure flow index and optical properties simultaneously to accurately extract blood flow information. This study provides unique insight through the use of liquid phantoms, hybrid instrumentation, incorporation of measurement errors and a generalization into DCS flow index errors due to the influences of optical properties.

KEYWORDS: Diffuse Correlation Spectroscopy, Diffusing Wave Spectroscopy, Near Infrared Spectroscopy, Tissue Optical Properties, Blood Flow

Daniel Irwin

7/27/2011

INFLUENCE OF TISSUE ABSORPTION AND SCATTERING ON
DIFFUSE CORRELATION SPECTROSCOPY BLOOD FLOW MEASUREMENTS

By

Daniel Irwin

<div style="text-align: right;">

Dr. Guoqiang Yu
Director of Thesis

Dr. Abhijit Patwardhan
Director of Graduate Studies

7/27/2011

</div>

RULES FOR THE USE OF THESES

Unpublished theses submitted for the Master's degree and deposited in the University of Kentucky Library are as a rule open for inspection, but are to be used only with due regard to the rights of the authors. Bibliographical references may be noted, but quotations or summaries of parts may be published only with the permission of the author, and with the usual scholarly acknowledgments.

Extensive copying or publication of the thesis in whole or in part also requires consent of the Dean of the Graduate School of the University of Kentucky.

A library that borrows this thesis for use by its patrons is expected to secure the signature of each user.

<u>Name</u>   <u>Date</u>

_____

_____

_____

_____

_____

_____

_____

_____

THESIS

Daniel Irwin

The Graduate School

University of Kentucky

2011

INFLUENCE OF TISSUE ABSORPTION AND SCATTERING ON
DIFFUSE CORRELATION SPECTROSCOPY BLOOD FLOW MEASUREMENTS

THESIS

A thesis submitted in partial fulfillment of the
requirements for the degree of Master of Science in Biomedical
Engineering in the Graduate School at the University of Kentucky

By

Daniel Irwin

Lexington, Kentucky

Director: Dr. Guoqiang Yu, Assistant Professor of Biomedical Engineering

Lexington, Kentucky

2011

ACKNOWLEDGMENTS

TABLE OF CONTENTS

LIST OF TABLES

LIST OF FIGURES

GLOSSARY

SYMBOLS

α	Ratio of Moving Scatterers to Total Scatterers
αD_B	*Effective* Diffusion Coefficient
β	Coefficient for Laser Stability, Coherence Length and # Speckles Detected
η	Viscosity
λ	Wavelength
μ_a	Absorption Coefficient
μ_s'	Reduced Scattering Coefficient
ρ	Source-Detector Separation
τ	Correlation Time
D	Photon Diffusion Coefficient
D_B	Diffusion Coefficient – Brownian in this Thesis
g_1	Normalized Electric Field Temporal Autocorrelation Function
G_1	Unnormalized Electric Field Temporal Autocorrelation Function
g_2	Normalized Light Intensity Temporal Autocorrelation Function
G_2	Unnormalized Light Intensity Temporal Autocorrelation Function
Hb	Deoxygenated Hemoglobin
HbO_2	Oxygenated Hemoglobin
k_0^2	Wavenumber
n	Ratio of Sample and Air Index of Refraction
$\left\langle \Delta r^2(\tau) \right\rangle$	Mean-Square Displacement of Scatterers during τ
$\vec{r}$	Position Vector
$S(\vec{r})$	Source Light Distribution
S_0	Source Light Intensity
T	Temperature
v	Speed of Light in Sample Medium

TERMS

APD	Avalanche Photodiode
ASL-MRI	Arterial Spin Labeled Magnetic Resonance Imaging
BFI	Blood Flow Index
CW	Continuous Wave
DCS	Diffuse Correlation Spectroscopy
DOCT	Doppler Optical Coherence Tomography
DWS	Diffusing Wave Spectroscopy
FD	Frequency Domain
IRB	Institutional Review Board
LDF	Laser Doppler Flowmetry
OMAG	Optical Microangiography
NIR	Near-Infrared
NIRS	Near-Infrared Spectroscopy
PAD	Peripheral Arterial Disease
PAT	Photoacoustic Tomography
PCS	Photon Correlation Spectroscopy
PET	Positron Emission Tomography
PMT	Photomultiplier Tube
rBF	relative Blood Flow
RBC	Red Blood Cells
RPM	Revolutions Per Minute
SNR	Signal-Noise Ratio
TD	Time-Domain
TRS	Time-Resolved Spectroscopy
Xe-CT	Xenon-enhanced Computed Tomography

CHAPTER 1: INTRODUCTION

1.1 Blood Flow Measurements

Blood flow is widely used as a physiological parameter in the assessment of multiple facets of disease including diagnosis [1] and treatment efficacies [2]. Analyses of blood flow extend into many applications. For example, the identification of blood flow abnormalities may be investigated for diseases such as peripheral arterial disease (PAD) [3]. The increase or decrease of blood flow to ischemic muscle tissue after surgical techniques can provide useful information as to the success of the procedures [3]. Monitoring blood flow may reveal benefits of particular treatment methods which are very important in studies involving tumors [1, 2, 4]. The tumor blood flow response to applications of radiation treatment to subjects with tumors can reveal if the treatment is working [2, 4]. The tumor site may also potentially be identified through exhibition of blood flow different from that of surrounding tissues [1]. Blood flow responses may also be followed after induced stimuli to examine activity of the brain [5].

In practice, blood flow measurements can be achieved through a variety of noninvasive technologies. Each has their own advantages and disadvantages and thus many factors must be considered including costs, portability, subject anatomy, accuracy, data acquisition time, and sensitivity. Sensitivity concerns the differentiation between vessels of varying sizes from large, such as arteries, to small such as capillaries. For superficial blood flow measurements (several μm to mm), technologies such as laser Doppler flowmetry (LDF) [6-8], optical microangiography (OMAG) [9], Doppler optical coherence tomography (DOCT) [10], and photoacoustic tomography (PAT) [11] may be

utilized. Penetration into deep tissues (e.g., several centimeters) is a limitation of employing these methods. Several modalities exist capable of penetrating into deep tissues such as Xenon-enhanced computed tomography (Xe-CT) and positron emission tomography (PET). While these are predominantly sensitive to microvasculature, they require the need for undesirable exposure to effects such as radiation. The applicability of using these deep penetration devices bedside is limited due to high costs and low portability. A new technology, near-infrared (NIR) diffuse correlation spectroscopy (DCS), has sought to fill some of the gaps in deep tissue microvasculature blood flow measurements by means of low cost, noninvasive, fast and portable instrumentation.

1.2 Near Infrared Diffuse Optical Techniques

Our investigations involve the use of NIR light to probe deep tissues. NIR light is employed in biomedical applications due to the discovery of a spectral (600 − 900 nm) window (see **Fig. 1**) in biological tissues [12]. This window allows deep penetration due to the low tissue absorption. Diffuse optical systems can be utilized for the extraction of information including tissue optical properties, oxygenated hemoglobin concentration (HbO$_2$), deoxygenated hemoglobin concentration (Hb), and blood flow [12, 13]. Note that tissue optical properties are represented by the absorption coefficient, μ_a (cm^{-1} units), and reduced scattering coefficient, μ_s' (cm^{-1} units). We will refer to diffuse optical equipment measuring μ_a, μ_s', HbO$_2$, and Hb as NIR spectroscopy (NIRS) and blood flow as DCS.

Typically, NIRS is separated into three paradigms: time-domain (TD) (additionally known as time-resolved spectroscopy, TRS), frequency-domain (FD), and continuous-

wave (CW). TD systems use light pulses and contain high information content but are expensive and complex [12, 13]. Modulated light from FD systems provide less information content than TD systems but are capable of separating μ_a and μ_s' and obtaining Hb and HbO_2 [12, 13]. The final paradigm employs a CW light source and is generally inexpensive and simple in comparison to the TD and FD paradigms. However, CW light provides limited information content making it difficult to decouple tissue optical properties [12, 13]. In this study we are only concerned with absolute μ_a and μ_s' from FD NIRS measurements.
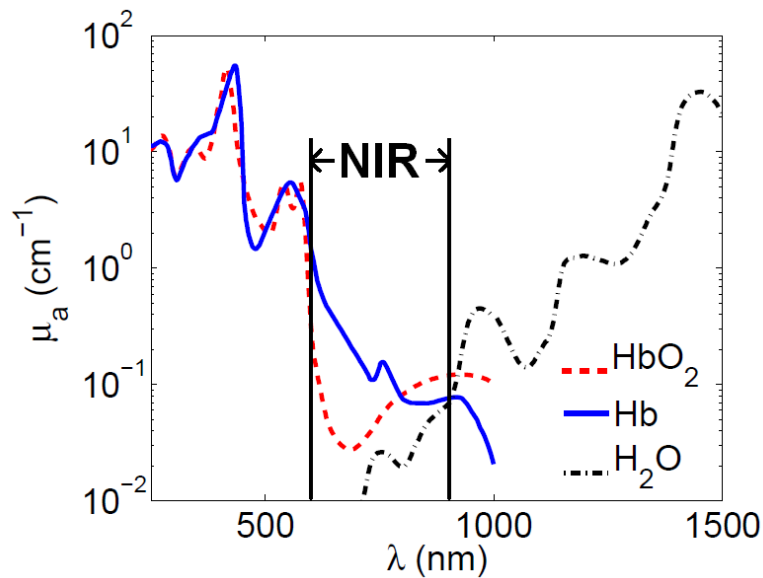
Figure 1. Spectral Window

The wavelength-dependent absorption coefficients (μ_a) shown for oxygenated hemoglobin (HbO_2), deoxygenated hemoglobin (Hb), and water (H_2O) with the NIR spectral window denoted with dashed lines for the wavelength range of 600 – 900 nm.

For NIRS measurements, a pair of source and detector optical fibers is placed on the tissue surface separated by a distance of up to a few centimeters. An NIR laser emits light

into tissue through the source fiber. Photon migrates in the tissue following a well-known diffusive process before being detected by a photodetector connected to the detector fiber [12, 14]. The tissue optical properties, μ_a and μ_s', represent the reciprocals of absorption and scattering length, respectively. The absorption length describes the distance a photon travels before encountering an absorption event and similarly for the scattering length corresponding to a scattering event. Note that the optical properties are wavelength, λ, dependent, i.e., μ_a (λ) and μ_s' (λ), but are written without the dependence notation throughout this paper. Light scattering in biological tissues is generally much greater than that of absorption resulting in diffusive behavior.

For the determination of particle dynamics (flow), speckle fluctuations in scattered light intensity are monitored [12, 13]. Previous success in flow measurements (e.g., laser Doppler) has been obtained in optically thin samples where single scattering photon correlation spectroscopy (PCS) can be assumed [13, 15, 16]. In probing the motions in thick/deep tissues, however, additional complications are encountered. Such optically thick tissue samples result in multiple scattering and randomization of light propagation. To address this multiple scattering problem DCS [14, 15, 17, 18], also known as diffusing wave spectroscopy (DWS) [5, 19], has been developed that takes advantage of the diffusive behavior of light as it propagates through the tissue.

1.3 Diffuse Correlation Spectroscopy (DCS)

DCS flow measurements are performed from the surface of the tissue region of interest, similar to NIRS. The flow measurements are obtained by monitoring the time autocorrelation function of speckle fluctuations detected at the photodetector. To

accomplish this, a long coherence length CW NIR laser is employed to provide a constant phase both spatially and temporally [12, 14, 16]. Speckle fluctuations in non-muscular biological tissues are primarily due to the movement of red blood cells (RBC's) in vessels [1, 2, 4, 5, 12, 18, 20-38]. However, motion artifacts and tissue shearing may arise in muscular tissues which may complicate measurements [39, 40]. DCS produces a blood flow index (BFI) and subsequent relative blood flow (rBF) from those fluctuations. The rBF produced from DCS measurements has been validated against other technologies in many tissues. These include comparisons with Xe-CT [23], Doppler ultrasound [20, 21], LDF [12], power Doppler ultrasound [4, 22], arterial spin labeled magnetic resonance imaging (ASL-MRI) [25, 41], fluorescent microsphere measurements [24], and to literatures [17, 18, 26, 27, 42]. DCS systems have had their usage expanded into many deep tissue applications including brain [5, 12, 18, 20, 21, 23-27, 29, 33-37], muscle [3, 39-41, 43, 44], and tumor [1, 2, 4, 22, 28, 30-32].

DCS can be made simple, inexpensive, and portable with short acquisition times (from 6.5 ms up to several seconds) such that bedside monitoring is made feasible [1, 27, 29, 39]. DCS is sensitive predominantly to microvasculature instead of the larger blood vessels. An inherent feature to using optical modalities is the noninvasive nature of measurements without the need for imposing undesirable effects such as radiation exposure. Spatial resolution is relatively low (~cm) governed by the volume probed where the penetration depth is approximately half of the separation between source and detector fibers. Thus, DCS fills a unique niche with the ability to simply and quickly monitor blood flow in deep tissues with robust applicability.

1.4 DCS Measurement Limitations and Current Study

Within the DCS theoretical framework, the BFI calculation has a dependence on tissue properties, μ_a and μ_s'. Thus, calculations in the DCS flow indices will be influenced by variations in these optical properties (see details in Chapter 2.1). An additional potential influence on the flow indices is the laser source wavelength chosen. As DCS requires a CW light source it is inherently incapable of monitoring absolute tissue optical properties during flow acquisition. Two general methods commonly serve as solutions to this dilemma: using separate instrumentation for monitoring the optical properties or making assumptions of their values. In some recent studies, hybrid instrumentation has been used to monitor both sets of information in order to establish accurate blood flow data [1, 2, 21, 39, 45]. This method may be costly or unavailable and in such cases requires making assumptions as to the optical properties of the particular tissue being investigated. In studies where assumptions in optical properties are made typically either the μ_s' is assumed constant while μ_a changes are measured [24, 36, 43] or the values for both μ_a and μ_s' are obtained from literatures for the respective tissue type (e.g., brain or tumor) [20, 40]. However, by making optical property assumptions there will be an increased susceptibility to longitudinal, transient, and inter-subject deviations from the assumed values or differences between literatures.

Another concern is that flow indices in DCS tissue measurements actually correspond to a calculated *effective* Brownian diffusion coefficient (see Chapter 2.1). This diffusion coefficient is considered to be different from the conventional Brownian diffusion coefficient as predicted by Einstein [46]. It has been determined empirically that dynamic scatterer motions (typically microvasculature RBC's) are best modeled by Brownian

diffusion rather than random ballistic flow, but the reasons for this are currently unknown [4, 12, 18, 20, 22, 28, 29, 36]. Thus, there is a lacking in some standard of comparison for the DCS flow index.

Currently, there has been no known generalization of potential DCS BFI errors due to inaccuracies in the estimation of the optical properties. A formal study is needed to elucidate upon the lack of optical property data while making DCS blood flow measurements. We have recently built a hybrid instrument in our lab capable of measuring flow indices using DCS and absolute μ_a and μ_s' using NIRS at several wavelengths simultaneously [44]. With this hybrid instrument we now have the capacity to evaluate and quantify optical property influences on DCS flow indices at different wavelengths. The FD NIRS system is incorporated to obtain the absolute μ_a and μ_s' at multiple wavelengths. These tissue optical properties are extracted from the modulated light AC, DC, and Phase information as it passes through the sample.

We have created homogeneous liquid phantoms allowing for manipulation of the optical property variations. NIRS and DCS techniques commonly employ liquid phantoms to emulate tissue for experimental and calibration purposes [13, 14, 18, 47-53]. Each parameter, either μ_a or μ_s', are varied individually to isolate their respective influence on DCS flow indices. By using liquid phantoms a standard for comparison with DCS is now possible. The phantoms include spherical particles suspended in liquid and undergoing Brownian motion as modeled by Einstein. Contrary to tissue, DCS measurements on these liquid phantoms should produce *effective* Brownian diffusion coefficients (i.e., DCS flow indices) which are now equivalent to the Einstein predictions. By utilizing this situation, the Brownian diffusion coefficient found using the Einstein-

Stokes formula [46] can be considered a true flow index. This can subsequently be used in comparison to DCS flow indices calculated using assumed or measured optical properties. Errors can then be determined in DCS flow indices due to the inaccurate optical property estimations at multiple wavelengths.

This study resolves the need for combining instrumentation to monitor both blood flow using DCS technology simultaneously with acquisition of tissue optical properties. We utilize liquid phantoms as a valuable means to investigate the influences of these optical properties on DCS flow indices. In addition, through comparisons of DCS flow indices with Brownian diffusion coefficients (true flow indices) we are capable of quantifying measurement errors in our system and methods. To further investigate the implications of the phantom study, a clinical study performed with the hybrid instrument for monitoring blood flow indices and optical properties of head and neck tumors is analyzed. Determination of *in-vivo* applicability involves ascertaining the measurement errors in tumor blood flow indices which are discussed and compared to the phantom study findings.

This thesis is organized into the following chapters. Chapter 2 opens with discussion of the theory used in DCS BFI calculations along with a brief overview of absolute μ_a and μ_s' measurements and hybrid instrument operation. Details pertaining to Brownian motion and liquid phantoms are also provided. The experimental protocols and methods of data analysis for the phantom study and *in-vivo* tumor study complete the chapter. The results of the phantom experiments and tumor study analysis are detailed in Chapter 3 with respective discussion and conclusions in Chapter 4. Finally, Chapter 5 presents the

novel contributions in this study along with directions for future research and investigations.

CHAPTER 2: METHODS AND MATERIALS

A hybrid NIR diffuse optical instrument combining a commercial frequency-domain NIR tissue-oximeter, the Imagent (ISS, Inc., IL, USA) [47, 48], and a custom-made NIR DCS flow-oximeter [3, 37, 44] was used in this study for simultaneous measurements of tissue optical properties and flow indices (see **Fig. 2**). The influences of optical properties on blood flow indices were examined in liquid phantoms with varied optical properties and in head and neck tumors using hybrid optical instruments. This chapter is organized as follows. First, the theories involved in obtaining DCS flow indices (i.e., *effective* Brownian diffusion coefficients) (Chapter 2.1) and tissue optical properties (i.e., μ_a and μ_s') (Chapter 2.2) are introduced along with the hybrid instrument data acquisition details (Chapter 2.3). Afterwards, the manner of determining Brownian diffusion coefficients (Chapter 2.4) is described. Next, the methods used for creating the liquid phantoms with varied optical properties are given (Chapter 2.5). Following is a discussion of the experimental protocols (Chapter 2.6) and data analysis (Chapter 2.7) in liquid phantoms. Finally, particulars concerning an analysis of real tissue data in a clinical study of head and neck tumors are provided (Chapter 2.8).
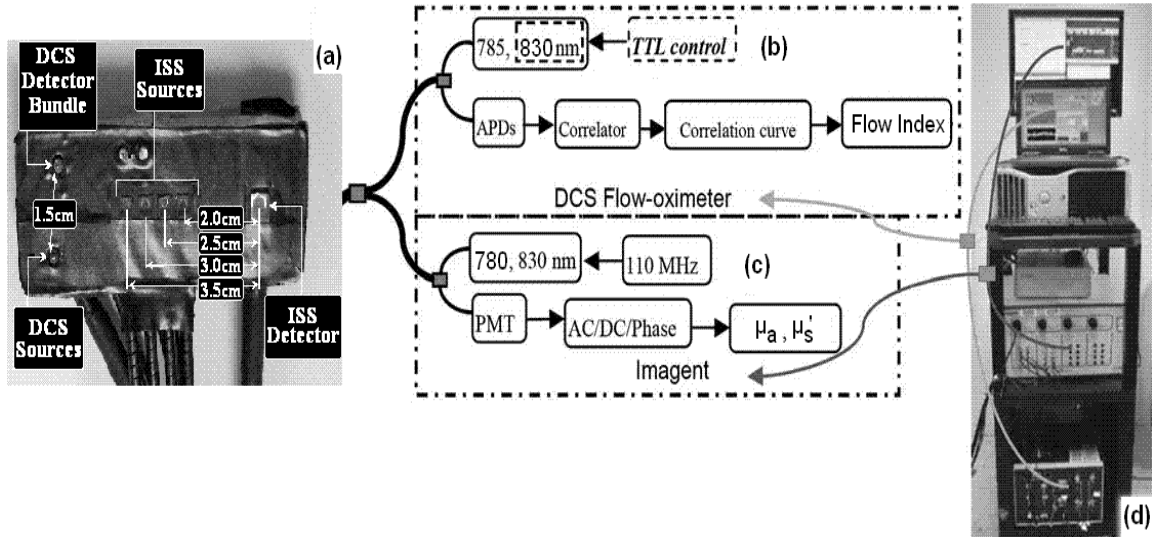
Figure 2. Hybrid Instrument

The combined Imagent and DCS hybrid instrument used during the phantom study with: (a) hybrid optical probe, (b) DCS flow-oximeter with 2 multi-mode laser source fibers (200 μm diameter) bundled together (785 and 830 nm) at 1.5 cm separation from 4 single-mode detector fibers (5.6 μm diameter) bundled together, (c) Imagent with 8 laser source fibers arranged as 1 per each wavelength at 4 separations (2.0, 2.5, 3.0, and 3.5 cm) of 780 and 830 nm along with 1 detector fiber, and (d) hybrid instrument. Note that two additional DCS detector fibers are shown, at 2.4 and 2.8 cm separations, but were not connected for this study.

2.1 Diffuse Correlation Spectroscopy (DCS) for Blood Flow Measurements

The dual-wavelength DCS system [44] with two long coherence length CW NIR laser sources at 785 and 830 nm (100 mW, Crystalaser, Inc., NV, USA) is used to quantify DCS flow indices from measurements on turbid samples such as biological tissues and liquid phantoms. DCS laser light is emitted into the tissue alternately by means of two multi-mode optical fibers (200 μm diameter). These fibers are bundled together on the tissue surface at the same position (see **Fig. 2**). Four single-mode detector fibers (5.6 μm diameter) are bundled and placed on the tissue surface as well with 1.5 cm separation

from the source fiber bundle, combined into a rectangular foam pad. Each detector fiber is connected to a single photon-counting avalanche photodiode (APD) (PerkinElmer, Inc., Canada). A 4-channel autocorrelator board (Correlator.com, NJ, USA) receives the outputs of the 4 APDs and produces normalized light intensity temporal autocorrelation functions (g_2). The g_2's from four detectors are averaged to improve the signal-noise-ratio (SNR). The averaged g_2 can then be related to the normalized electric field temporal autocorrelation function (g_1) through the Siegert relation [54],

$$g_2(\vec{r}, \tau) = 1 + \beta |g_1(\vec{r}, \tau)|^2 \qquad (1)$$

where τ is the delay time, $\vec{r}$ is the position vector, and β depends on laser stability and coherence length and the number of speckles detected.

Although in practice DCS measures g_2, the analytical solution is for g_1 derived from the transport of the unnormalized temporal electric field correlation function (G_1) through the turbid sample. The moving scatterers will contribute to the exponential decay of G_1. The transport of G_1 results in the following correlation diffusion equation, derived rigorously elsewhere [13, 14], for homogeneous media with a CW source (steady state):

$$\left(D\nabla^2 - v\mu_a - \frac{1}{3}v\mu_s' k_0^2 \alpha \langle \Delta r^2(\tau) \rangle \right) G_1(\vec{r}, \tau) = -vS(\vec{r}) \qquad (2)$$

where $D = v/(3\mu_s')$ is the photon diffusion coefficient, v is the speed of light in the medium, k_0^2 is the wavenumber, $S(\vec{r})$ is the source light distribution, and $\langle \Delta r^2(\tau) \rangle$ is the mean-square displacement of scatterers in time τ. The position vector, $\vec{r}$, denotes a general vector from a source to a point of detection. Notice that g_1 is the normalized form of G_1, as used in Eq. 1, i.e., $g_1(\vec{r}, \tau) = G_1(\vec{r}, \tau)/G_1(\vec{r}, 0)$.

12

The homogeneous CW solution to Eq. 2 for semi-infinite geometry is (see **Fig. 3**):

$$G_1(\rho,\tau) = \frac{vS_0}{4\pi D}\left(\frac{\exp(-K(\tau)r_1)}{r_1} - \frac{\exp(-K(\tau)r_2)}{r_2}\right) \qquad (3)$$

where S_0 is the source intensity, ρ is the separation distance between source and detector,

$K^2(\tau) = 3\mu_a\mu_s' + \mu_s'^2 k_0^2 \alpha \langle \Delta r^2(\tau) \rangle$, $r_1 = \left[\rho^2 + (z-z_0)^2\right]^{1/2}$, $r_2 = \left[\rho^2 + (z+z_0+2z_b)^2\right]^{1/2}$, $z_0 = 1/\mu_s'$,

$z_b = 2(1+R_{eff})/3\mu_s'(1-R_{eff})$, $R_{eff} = -1.440\ n^{-2} + 0.710\ n^{-1} + 0.668 + 0.0636\ n$, and $n \approx 1.33$

(for phantoms and tissues) [12, 13, 55, 56]. The R_{eff} term accounts for the mismatch between the medium and air index of refraction with n being the ratio between them.

The collimating laser source is placed at (0, 0, 0) and detector at (ρ, 0, 0) on the tissue surface with z = 0 (see **Fig. 3**) for semi-infinite geometry. The solution (Eq. 3) involves an isotropic source at z = z_0 and negative isotropic imaging source at z = -(z_0 + 2z_b) with an extrapolated zero boundary condition. The position vector, $\vec{r}$, from Eq. 2 regards the point source at (0, 0, z_0) and negative imaging source at (0, 0, -(z_0 + 2z_b)). The superposition of solutions to these two sources with infinite geometry provides the resulting Eq. 3 where now the semi-infinite boundary is modeled by the scalar parameter, ρ. Further details are given elsewhere [13, 56].

The movement of scatterer particles is typically characterized for biological tissues by Brownian motion with $\langle \Delta r^2(\tau) \rangle = 6D_B\tau$, where D_B is the *effective* Brownian diffusion coefficient. In order to differentiate static and dynamic scatterer particles, an α (0 − 1) term is added. This term is defined as the ratio of dynamic to total scatterers from the sample. The BFI produced by DCS in tissues is defined as the combined dynamic scatterer ratio with the *effective* Brownian diffusion coefficient, i.e., αD_B. The BFI can then be used to determine the rBF by comparison with the baseline BFI, BFI$_{Baseline}$, prior

to any physiological changes, i.e., $\mathrm{rBF} = \mathrm{BFI}/\mathrm{BFI}_{\mathrm{Baseline}}$. In tissue samples, scatterers may be static (e.g., mitochondria, organelle) or dynamic (RBC). However, in liquid phantom solutions (see Chapter 2.5) all scatterers are dynamic resulting in $\alpha \approx 1$. Thus, the DCS flow indices in this thesis related to the phantom study are reported as just D_B.
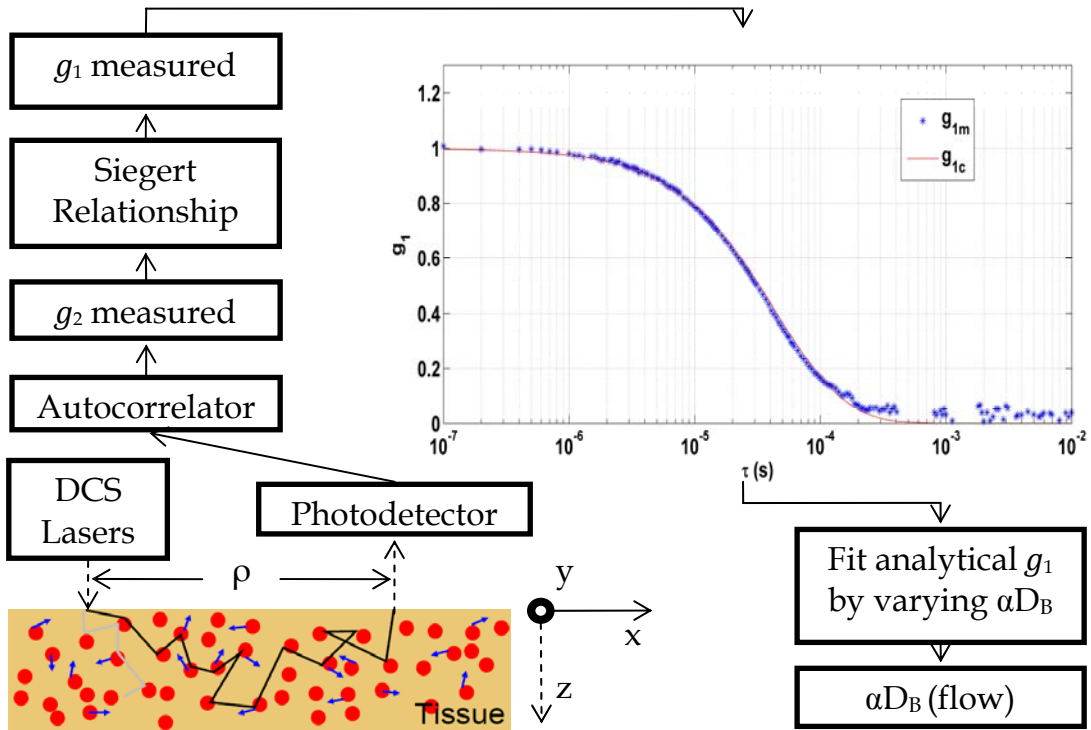
Figure 3. DCS Data Acquisition

The process of DCS data acquisition beginning with tissue measurement (bottom left) and ending with (bottom right) production of a DCS flow index (αD_B). Cartesian coordinates are shown with respect to DCS source-detector and tissue orientation with the y-axis directed into the page. A typical correlation curve is shown as an example, taken from a phantom experiment (μ_a (830 nm) = 0.05 cm^{-1}, μ_s' (830 nm) = 10 cm^{-1}) with g_1 derived from g_2 measurements (g_{1m}) using Eq. 1 and g_1 calculated (g_{1c}) using Eq. 3.

To quantify a flow index, $g_2(\vec{r}, \tau)$ is first obtained for a given sampling time (~44 ms) from the correlator where the sample is illuminated by a DCS source (either 785 or

830 nm). Multiple samples are obtained and averaged during a measuring time of ~1.2 s. From Eq. 1, β is found at $\tau \approx 0$ using measured $g_2(\rho,0)$ and $g_1(\rho,0) \approx 1$ (i.e., $g_1(\rho,0) = G_1(\rho,0)/G_1(\rho,0) = 1$). This leads to $\beta = g_2(\rho,0) - 1$. It is assumed that β will remain constant throughout the remaining τ since it only depends on the optical system [15]. Now, $g_1(\rho,\tau)$ can be calculated for all τ with Eq. 1 using measured $g_2(\rho,\tau)$ and calculated β. The flow index (αD_B) is then considered an unknown parameter in Eq. 3, which is fit with the $g_1(\rho,\tau)$ calculated previously. For each DCS data acquisition sequence, a unique flow index is obtained for 785 and 830 nm. Two flow indices are obtained sequentially to obtain a complete frame of DCS data acquisitions at two wavelengths. The overall process of DCS data acquisition is given in **Fig. 3**.

2.2 Frequency Domain Spatially Resolved Near-Infrared Spectroscopy for Measurement of Optical Properties

A four-wavelength (690, 750, 780, and 830 nm) FD multi-distance spatially resolved spectroscopy instrument, i.e., the Imagent, is incorporated to quantify absolute μ_a and μ_s'. Only two wavelengths (780 and 830 nm) were chosen so as to match the available DCS lasers (785 and 830 nm). Imagent measurements are obtained similar to DCS with semi-infinite geometry, by emitting NIR light into the tissue through source fibers with detector fibers up to a few cm away, both at the tissue surface. The FD Imagent system emits light sinusoidally modulated at 110 MHz. Optical fiber arrangement consists of 8 source fibers (4 per wavelength) placed at four pre-determined distances (2.0, 2.5, 3.0, and 3.5 cm) from a detector fiber bundle. The detector fiber is connected to a photomultiplier tube (PMT) (see **Fig. 2**). Utilizing the amplitudes of light signal

modulation (ac), average (dc), and phase (φ), information can be detected from the different source-detector separations (r). It was found that linear relationships exist between logarithmic ac, logarithmic dc or φ and the spatial distances through solutions to a photon diffusion equation [48]. The slopes (Sl_{ac}, Sl_{dc}, $Sl_{φ}$) of these linear relationships can be fit from the multi-distance measurements. From these slopes $μ_a$ and $μ_s$' can be determined at both wavelengths. For the phantom study, by use of homogeneous phantoms the different source and detector separations are expected to have minimal effect on the measured optical properties despite probing different depths. In the real tissue tumor study analysis this effect may be more prominent (see Chapter 3.4).

In Imagent operation, the fitting solutions mentioned above are not ideal for real tissue measurements due to the requirement of iterative calculations. Therefore, a faster approximate solution is employed defined by the following equations [57]:

$$\ln\left(dc\ r^2\right) = rSl_{dc}\left(μ_a, μ_s'\right) + In_{dc}'\left(D, K_{dc}\right) \tag{4}$$

$$\Phi = rSl_{\Phi}\left(μ_a, μ_s', ω, v\right) + In_{\Phi}'\left(K_{\Phi}\right) \tag{5}$$

$$\ln\left(ac\ r^2\right) = rSl_{ac}\left(μ_a, μ_s', ω, v\right) + In_{ac}'\left(D, K_{ac}\right) \tag{6}$$

where ω is the angular frequency of the modulation, v is the speed of light in the medium, D is the photon diffusion constant ($D \approx 1/3μ_s'$), K_{Φ} is the relative phase of the source plus any phase shifts outside the sample, K_{ac} and K_{dc} are constants dependent on detector sensitivity factors, modulation depth, and source intensity, and In'_{dc}, In'_{Φ}, and In'_{ac} are the line intercepts. Only two of the three slopes are required per wavelength to obtain corresponding $μ_a$ and $μ_s$', but using the combination of Sl_{ac} and Sl_{Φ} eliminate influences form background light [47].

2.3 Hybrid Instrument Data Acquisition

The hybrid instrument alternates data acquisition sequentially between DCS and Imagent. An individual acquisition sequence begins with DCS activating the first laser and collecting data from the autocorrelator. The first laser is then switched off and the process is repeated for the second DCS laser. Notification is then sent from DCS to the Imagent via a TTL trigger to proceed with an iteration of data acquisition. The Imagent activates an individual laser source at the first distance collecting data from the PMT. Data is collected similarly for the Imagent laser activated alternately at each distance. The Imagent laser is then shut off and each remaining Imagent laser source (at different wavelengths) is sequentially activated to acquire data in the same manner before finally returning control to the DCS. The notification to DCS signifies the completion of one data acquisition cycle, which is then repeated until the end of the measurement. Total data acquisition time per frame is ~2.7 s (~1.2 s for each of two DCS wavelengths and ~0.3 s for Imagent). After the measurement is finished Imagent places AC, DC, and Phase information into a .txt file. The .txt file is further analyzed by supplemental Imagent processing functions, such as to produce μ_a and μ_s', and saved in a .log file.

2.4 Particle Brownian Motion in Liquid Phantoms

For comparisons with DCS flow indices, Einstein Brownian diffusion coefficients are determined for liquid phantoms. Intralipid particles provide Brownian motion within the phantoms. This motion is expected to be equivalent to the *effective* Brownian diffusion coefficient (flow index) as measured using DCS [46]. Determination of the phantom diffusion coefficient follows calculations per the Einstein-Stokes formula for spherical particles suspended in liquid defined as:

$$D_B = \frac{k_B T}{6\pi R \eta} \tag{7}$$

where R is the Intralipid spherical particle radius, η is the viscosity of the phantom, T is the temperature of the phantom, and k_B is the Boltzmann constant [46]. Due to difficulties in measuring the Intralipid particle radius, an estimation of 196 nm is used (see Chapter 2.7). The phantom viscosity is measured with a commercial viscometer (Brookfield, MA, USA). The viscosity parameter is reported in units of cP (centipoise), where 1 cP = 1 mPa·s (millipascal·second) = 0.001 kg·m^{-1}s^{-1} [58]. Measurement of the phantom temperature is obtained via a temperature sensor (Physitemp, NJ, USA) attached near the hybrid probe. For further details on acquisition of this data see Chapter 2.6.

2.5 Liquid Phantom Creation

We follow previously published methods for creating liquid phantoms, but examine implementation details thereof here for clarity and re-creation purposes. The composition of liquid phantoms consist of India ink (Black India 44201, Higgins, MA, USA), Intralipid (30%, Fresenius Kabi, Uppsala, Sweden), and distilled water. Originally deionized water was used, but was difficult to obtain and produced similar results to

distilled water for our purposes. The complete liquid phantom setup can be seen in **Fig. 4**. The phantom solution is contained within a 9607.5 cm^3 aquarium (~9.5 L). The hybrid fiber-optic probe (see **Fig. 2**) is positioned on the phantom surface simulating superficial tissue measurement configuration of semi-infinite geometry. To keep the probe stationary, a custom probe holder was built by a machine shop. The holder maintains the probe near the center of the phantom solution, away from aquarium boundaries.
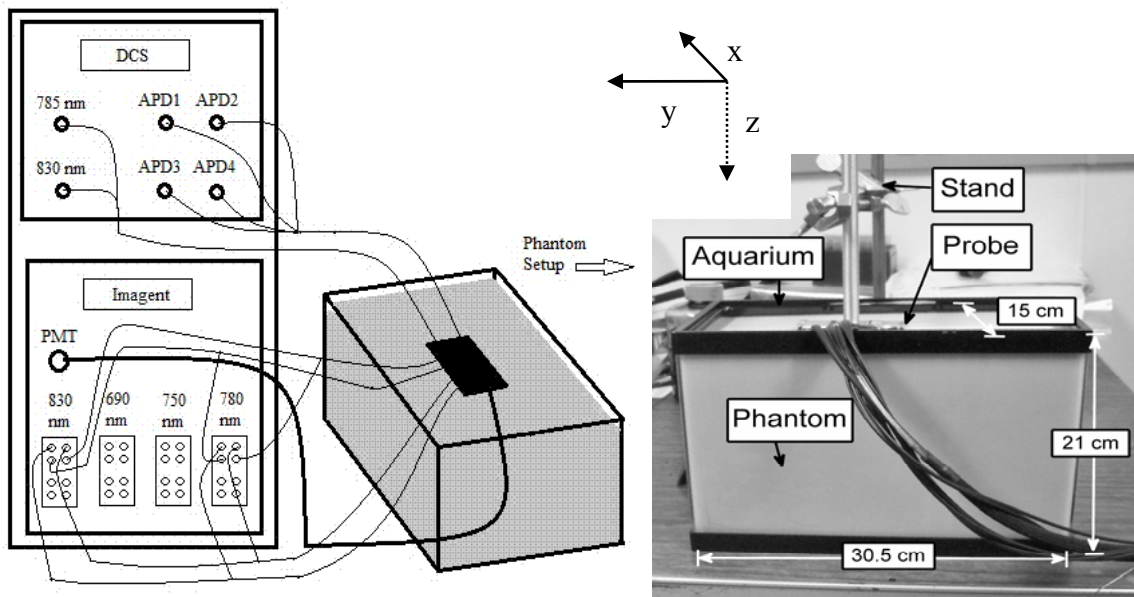
Figure 4. Liquid Phantom Setup

Hybrid instrument (left) and liquid phantom (right) setup including: ~9.5 L glass aquarium (30.5 cm x 21.0 cm x 15.0 cm), hybrid optical probe with holder, lab stand and Cartesian coordinates oriented for DCS source and detector.

A 30% Intralipid solution provides particle Brownian motion, as described by Eq. 7. Additionally, it is used to manipulate the phantom reduced scattering coefficient, μ_s' phantom, while contributing minimally to phantom absorption. The phantom absorption

coefficient, $\mu_{a\ phantom}$, is manipulated using the India ink with minimal influence on phantom scattering. Due to the very high contribution of absorption from pure India ink, a solution of 10% ink with 90% distilled water is created. The 10% solution is used rather than pure ink to manipulate the $\mu_{a\ phantom}$. Distilled water contributes little to both phantom absorption and scattering, allowing for larger phantom volumes to facilitate satisfying the semi-infinite geometry model. The subscripts "water", "ink", and "Intralipid" denote distilled water, 10% ink solution, and 30% Intralipid, respectively. Prior to prediction of phantom optical properties, the μ_a and μ_s' of the contributing solutions must first be determined. These values will then be used in combination with titration equations for predicting the volumes of water, 10% ink solution, and 30% Intralipid needed to obtain the phantom optical properties required.

Intralipid, ink, and water μ_a. Spectrometer (Beckman Coulter, CA, USA) measurements allow derivation of the 10% ink solution absorption coefficient, $\mu_{a\ ink}$. The 10% ink solution is not within the measurable range of the spectrometer. Thus, for absorbance measurements the 10% solution is further diluted to a 0.025% ink solution (of ink and water). Multiple samples of the 0.025% ink solution are distributed into individual 1 cm path-length cuvettes and scanned by the spectrometer at 780 and 830 nm (matching the Imagent source wavelengths). These absorbances are averaged and converted to absorption by: $\mu_{a\ ink}(\lambda) = \ln(10) \times Absorbance(\lambda)$ [59]. Values for $\mu_{a\ water}$ at 780 and 830 nm are obtained from the literature [60]. As Intralipid is primarily comprised of water, it is assumed to have an absorption coefficient equivalent to water, i.e. $\mu_{a\ Intralipid} = \mu_{a\ water}$.

Intralipid, ink, and water μ_s'. The μ_s' of 30% Intralipid is derived from the theoretical values for 10% Intralipid. The μ_s' of 10% Intralipid is first calculated using a Mie theory approximation and subsequently multiplied by a factor of three to obtain the μ_s' of 30% Intralipid, μ_s' $_{Intralipid}$ [59]. The Intralipid particle radius and refractive index along with related theory and details are described in the original derivation [61], which has been used extensively for quantification of Intralipid-based liquid phantoms [12, 14, 59, 62, 63]. As there are expected to be no contributions to the phantom scattering by the 10% ink solution or distilled water both are ignored in calculations, i.e., μ_s' $_{ink}$ = μ_s' $_{water}$ = 0 cm^{-1}.

Liquid phantom μ_a variation. A list of desired μ_a and a constant μ_s' must first be chosen at a specific wavelength for creating phantoms with varied μ_a (see Chapter 2.6). Optical properties at other wavelengths are found later, once the phantom composition has been predicted. The available aquarium size is considered the total phantom volume, $V_{phantom}$. Volumes of distilled water (V_{water}), 10% ink solution (V_{ink}), and 30% Intralipid ($V_{Intralipid}$) required to obtain the set of μ_a and μ_s' are then calculated for the initial phantom. For our experiments, the initial phantom optical properties at 830 nm are: μ_a $_{phantom}$ (830 nm) = 0.05 cm^{-1} and μ_s'$_{phantom}$ (830 nm) = 10 cm^{-1}. Using a titration equation, the 10% ink solution volume (V_{ink}) can be determined as follows [59]:

$$\mu_{a\ water}(830nm) \times (V_{phantom} - V_{ink}) + \mu_{a\ ink}(830nm) \times V_{ink} = \mu_{a\ phantom}(830nm) \times V_{phantom}$$

$$(8)$$

The volume of 30% Intralipid ($V_{Intralipid}$) is determined using a similar titration equation [59],

$$\mu'_{s\ Intralipid}(830nm) \times V_{Intralipid} = \mu'_{s\ phantom}(830nm) \times V_{phantom} \qquad (9)$$

The volume of distilled water is simply the remaining volume to be filled, calculated by: $V_{water} = V_{phantom} - V_{ink} - V_{Intralipid}$. The 10% ink solution will be added in equivalent amounts each step to increase the phantom μ_a. Generalizing the titration equation to the volume of 10% ink solution to add, V_{ink}^{add}, is given by [59]:

$$\mu_{a\ phantom}^{i-1}(830nm) \ x \ V_{phantom}^{i-1} + \mu_{a\ ink}(830nm) \ x \ V_{ink}^{add} = \mu_{a\ phantom}^{i}(830nm) \ x \ \left(V_{phantom}^{i-1} + V_{ink}^{add}\right)$$

$$(10)$$

where i is the step (i.e., i = current step, i-1 = previous step). Notice that the total phantom volume for the next step will be the sum of the 10% ink solution volume added with the current volume. After the volumes have been determined Eq. 8 and Eq. 9 can be used with known volumes and constituent optical properties to predict the $\mu_{a\ phantom}(\lambda)$ and $\mu_{s}'_{\ phantom}(\lambda)$ at other desired wavelengths.

Liquid phantom μ_s' variation. The process for varying the phantom μ_s' is like that of μ_a variation, starting with selection of the constant μ_a and list of μ_s' (see Chapter 2.6). The initial phantom is created from the volumes of distilled water, 10% ink solution, and 30% Intralipid as calculated using Eq. 8 and 9. The desired initial phantom optical properties are: $\mu_{a\ phantom}(830\ nm) = 0.125\ cm^{-1}$ and $\mu_s'_{phantom}(830\ nm) = 4\ cm^{-1}$. Contrary to the μ_a variation, both 30% Intralipid and 10% ink solution need to be added at each step for μ_s' variation. The additional 30% Intralipid each step contributes additional volume and lowers the phantom absorption. To account for these factors requires matching the μ_a of the added 30% Intralipid to that of the phantom. This will maintain a constant phantom μ_a. The volume of 30% Intralipid to be added ($V_{Intralipid}^{add}$) is determined by the following titration equation [59]:

$$\mu'^{\,i-1}_{s\,phantom}\left(830nm\right)\ \times\ V_{phantom} + \mu'_{s\ Intralipid}\left(830nm\right)\ \times\ V^{add}_{Intralipid}$$

$$= \mu'^{\,i}_{s\,phantom}\left(830nm\right)\ \times\ \left(V_{phantom} + V^{add}_{Intralipid}\right) \tag{11}$$

The quantity of 10% ink solution to be added (V^{add}_{ink}) is determined by a slightly modified form of Eq. 10 [59],

$$\mu^{i-1}_{a\ phantom}\left(830nm\right)\ \times\ V_{phantom} + \mu_{a\ ink}\left(830nm\right)\ \times\ V^{add}_{ink} + \mu_{a\ water}\left(830nm\right)\ \times\ V^{add}_{Intralipid}$$

$$= \mu^{i}_{a\ phantom}\left(830nm\right)\ \times\ \left(V_{phantom} + V^{add}_{ink} + V^{add}_{Intralipid}\right) \tag{12}$$

Once the additional volumes of 10% ink solution and 30% Intralipid are added and mixed with the phantom solution, an equivalent volume to that added ($V_{remove} = V^{add}_{Intralipid} + V^{add}_{ink}$) is removed to maintain probe submersion depth. These procedures are repeated for all remaining steps. To predict the optical properties at other wavelengths, the percentage of each constituent must first be determined. It is assumed the percentages are equivalent in the amount of volume removed as to the entire phantom. This allows one to obtain their corresponding volumes at every step. Then Eq. 8 and 9 are used as is done with μ_a variation to predict the $\mu_{a\ phantom}(\lambda)$ and $\mu_{s}'{}_{phantom}(\lambda)$ at desired wavelengths.

2.6 Phantom Experimental Protocols

μ_a variation. In the first experiment, the μ_s' was maintained constant throughout: μ_s' (830 nm) = 10 cm^{-1}. Conversely, μ_a was varied in an increasing manner consisting of thirteen steps. The absorption range covers μ_a (830 nm) from 0.05 to 0.20 cm^{-1} with a step size of 0.0125 cm^{-1} (i.e., μ_a (830 nm) = 0.05, 0.0625, 0.075, …, 0.20 cm^{-1}). Calibration of the Imagent with a phantom of known optical properties is done prior to

starting measurements. During calibration, corrections are made accounting for the efficiency of optical coupling among the lasers/detector, optical fibers, and phantom [47, 57]. A liquid phantom of equivalent composition and optical properties as the midpoint (step 7) was used for calibration. The initial phantom was created consisting of optical properties at the lowest step, i.e., μ_a (830 nm) = 0.05 cm^{-1}. The hybrid probe with temperature sensor was placed onto this phantom and the following actions were taken for each of the 13 steps. The volume of 10% ink solution to add was determined as detailed in Chapter 2.5. This volume was then added to the liquid phantom via a pipette, mixed, and left to settle for 10 minutes while the optical properties and flow stabilized. During the 10 minute period three 500 μL samples were extracted from the phantom for viscosity measurements. The samples were taken from the right, middle, and left of the solution to minimize spatial variations. The pipette sampled from within 1-2 cm of the surface to prevent submersion. All lights in the room were switched off or covered with black tape. Black plastic was used to cover the phantom setup to reduce any remaining ambient light. Hybrid optical measurements (including temperature) were obtained for an interval of 5 minutes duration.

μ_s' variation. The second experiment maintained a constant μ_a throughout: μ_a (830 nm) = 0.125 cm^{-1}. The μ_s' was increased over a total of thirteen steps. The scattering range covers μ_s' (830 nm) from 4 to 16 cm^{-1} with a step size of 1 cm^{-1} (i.e., μ_s' (830 nm) = 4, 5, 6, …, 16 cm^{-1}). This experiment immediately followed the μ_a variation. Prior to instantiating this second phase, the μ_a variation phantom was disposed of and replaced by the μ_s' variation initial phantom. Alcohol pads were used to clean the probe before repositioning it onto the initial phantom. The DCS and Imagent were not shut down

between protocols. Two potential difficulties arise with the addition of 30% Intralipid due to the amount required: potential reduction in the phantom μ_a and probe submersion. The addition of 10% ink solution with that of the additional 30% Intralipid allows the μ_a of the phantom to be maintained. To prevent probe submersion, after mixing at each step an equivalent amount of phantom solution is removed. Hybrid optical, temperature, and viscosity measurements were obtained in the same manner as during μ_a variation.

2.7 Phantom Data Analysis

For each 5 minute interval, the following parameters were obtained through measurements and post-analysis calculations: μ_a, μ_s', temperature, viscosity, and three diffusion coefficients (D_B's). Note that in all cases except viscosity, data between intervals (i.e., making additions, stirring) is not included in data analysis. Interval averages were found for μ_a and μ_s' at both wavelengths (780 and 830 nm) over each 5 minute interval. Temperature is also averaged over each 5 minute interval. Viscosity measurements were obtained at 50, 60, and 100 RPM for each of three samples and averaged. The liquid phantom was assumed a Newtonian fluid. The three sample average was then calculated to produce the mean viscosity per interval. Using the averaged μ_a and μ_s' as known parameters DCS measured g_1's, calculated from Eq. 1 with measured g_2, are fit using Eq. 3 to produce two distinct D_B's. Subscripts denote which set of optical properties (assumed or measured) were used in order to differentiate the two D_B's. For assumed optical properties, the averaged μ_a and μ_s' from the middle interval (step 7), i.e., μ_a (830 nm) = 0.125 cm^{-1} and μ_s' (830 nm) = 10 cm^{-1}, are used in calculations of the first DCS D_B, termed $D_{B\text{-mid}}$. The $D_{B\text{-mid}}$ represents the diffusion coefficient without

consideration as to any optical property variations. Errors are induced in flow index calculations by forcing the varying optical property to be held constant. During early intervals the middle interval overestimates μ_a (first experiment) and μ_s' (second experiment) while at later intervals it underestimates. Corresponding interval μ_a and μ_s' averages are used in calculation of the second DCS D_B, termed $D_{B\text{-dynamic}}$. This D_B is considered the best evaluation of DCS flow index. $D_{B\text{-mid}}$ and $D_{B\text{-dynamic}}$ are calculated at both DCS wavelengths used, 785 and 830 nm. The DCS D_B calculations at 785 and 830 nm utilized the averaged optical property data from the Imagent at 780 and 830 nm, respectively. The influence from wavelength mismatch between 780 and 785 nm is considered to be minor. The two sets of DCS D_B's, at each wavelength, are calculated then averaged over the 5 minute interval. A third D_B is calculated by Eq. 7, termed $D_{B\text{-Einstein}}$, with the three sample averaged viscosity, interval averaged temperature, and estimated particle radius. The Intralipid particle radius estimation was found to exhibit the least errors between the measured DCS flow indices ($D_{B\text{-dynamic}}$) and calculated $D_{B\text{-Einstein}}$ at the calibration point (step 7). This estimation, 196 nm, is within the Intralipid particle size range as reported in the literatures [14, 61].

Figures and tables are used for results presentation to visualize measurement variations, optical property influences on DCS flow indices, and differences between predicted and measured values. Error bars illustrate standard deviations (SD) and data are depicted as mean ± SD. Percentage errors between measured and predicted values were calculated and used to characterize measurement errors. Student t-test p-values are presented to compare measurement errors, while the significance criterion is $p < 0.05$.

2.8 Head and Neck Tumor Study Protocol and Data Analysis

The phantom study results provide a general view of errors in flow indices due to constant optical properties assumptions. In order to more easily visualize the implications of such assumptions on real tissue measurements, *in-vivo* data from an ongoing tumor study is analyzed. A hybrid optical instrument, similar to that in the phantom study, was employed in measuring tissue hemodynamic properties of head and neck tumors in 10 patients. Inclusion was restricted to only those patients with Stage III-IVb Squamous Cell Carcinoma of the Head and Neck (SCCHN). Further selection criteria included neck lymph nodes that measured greater than 1 cm and were clinically thought to be involved by tumor. Subjects completed consent forms and institutional review board (IRB) approval was given by the University of Kentucky prior to participation in the study.

Not all DCS and Imagent laser sources used in the phantom study were available for the tumor study and, as a result, some differences are encountered. DCS employed lasers at 785 and 854 nm whereas the Imagent had 690 and 830 nm. The best match between source wavelengths of the two instruments, for data analysis, was determined to be 854 nm for DCS and 830 nm for Imagent. Due to the large gap between the other two sources, 785 versus 690 nm, they are excluded from this analysis. The Imagent source and detector fiber separations are identical as that in the phantom study (i.e., 2.0, 2.5, 3.0, and 3.5 cm). Three source and detector separations were achieved with DCS, utilizing 3 detector fibers at 1.5, 2.4, and 2.8 cm from the bundled source fibers. For the phantom study, homogeneity was assumed for all source and detector separations. However, in the tumor study our analysis focuses on the 2.8 cm separation from DCS as it is expected to be most comparable to the tissue region/depth probed by the Imagent. The handheld

probe was placed on the tissue surface at the center of the area identified as tumor node, as applicable to the semi-infinite geometry model, and secured in position. DCS flow indices and optical property data were acquired for a duration of ~2 minutes.

Optical properties were obtained by Imagent, as done in the phantom study, and averaged over the 2 minute measurement interval for the 10 patients. Calculations with four different sets of measured optical properties produced four unique DCS flow indices. The true DCS flow index is considered that which is calculated with the true corresponding patient μ_a and μ_s' (i.e., averaged Imagent data over 2 minutes), and is termed $\alpha D_{B\text{-dynamic}}$. The remaining three DCS flow indices are calculated using the overall patient minimum, mean, and maximum optical properties, termed $\alpha D_{B\text{-min}}$, $\alpha D_{B\text{-mean}}$, and $\alpha D_{B\text{-max}}$, respectively. These D_B estimates are compared with the true flow index, $\alpha D_{B\text{-dynamic}}$, for determining errors. Error bars in figures correspond to SD, and data are presented by interval mean $\pm$ SD.

CHAPTER 3: RESULTS

Presentation of results is ordered as follows. First, data related to the calculations of Brownian diffusion coefficients ($D_{B\text{-Einstein}}$) and DCS flow indices are given for μ_a variation in liquid phantoms (Chapter 3.1). In a similar fashion, these findings from μ_s' variation are then reported (Chapter 3.2). The next section (Chapter 3.3) summarizes the influence of μ_a and μ_s' variations on flow indices and is divided into three subsections: the influence of μ_a and μ_s' variations on $D_{B\text{-Einstein}}$, the measurement errors found for μ_a, μ_s' and DCS flow indices compared to predicted values, and the influence of inaccurate estimations of μ_a and μ_s' on DCS flow indices. Finally, the influence of tissue optical properties on DCS blood flow indices of head and neck tumors is presented (Chapter 3.4).

3.1 μ_a Variation

The first experiment performed consists of varying the μ_a of a liquid phantom while maintaining a constant μ_s' to evaluate the influences on DCS flow indices. Thirteen steps, with a μ_a step size of 0.0125 cm^{-1}, were carried out over μ_a (830 nm) from 0.05 to 0.20 cm^{-1} with μ_s' (830 nm) = 10 cm^{-1}. At 780 nm, the μ_a will also increase and have constant μ_s', but manipulations were purposely invoked at 830 nm only. Measurements were obtained for thirteen separate 5 minute intervals. These were analyzed post measurement producing data sets of mean and SD's per interval for viscosity, temperature and three D_B's. The viscosity, temperature and true flow index, calculated $D_{B\text{-Einstein}}$, are shown in **Fig. 5 – 7**, respectively, with error bars designating the SD's. Each $D_{B\text{-Einstein}}$ (**Fig. 7**) is

calculated with the measured interval temperature (**Fig. 6**), corresponding viscosity (**Fig. 5**), and estimated particle radius (196 nm).

Raw data and interval means with SD's (as error bars) of measured and true μ_a, μ_s', $D_{B\text{-Einstein}}$, $D_{B\text{-mid}}$, and $D_{B\text{-dynamic}}$ during μ_a variation at the employed wavelengths are displayed in **Fig. 8 − 14**. For raw data figures (**Fig. 8**, **10**, **12**, and **13**), the black vertical lines indicate separation between 5 minute data acquisition intervals and frame numbers serve as a generic counter as the data between intervals has been excluded for clarity. To quantify measurement errors for the optical properties, predictions using Mie theory estimations and spectrometer results are used as true values for comparisons to μ_s' and μ_a, respectively. Calculated $D_{B\text{-Einstein}}$ is not wavelength dependent and thus is the same for comparisons with DCS flow indices, $D_{B\text{-dynamic}}$ and $D_{B\text{-mid}}$, at both wavelengths. Averaged optical properties at the middle interval [μ_a (830 nm) = 0.125 cm^{-1} and μ_s' (830 nm) = 10 cm^{-1}] are used for calculations of $D_{B\text{-mid}}$ and from corresponding intervals for $D_{B\text{-dynamic}}$.
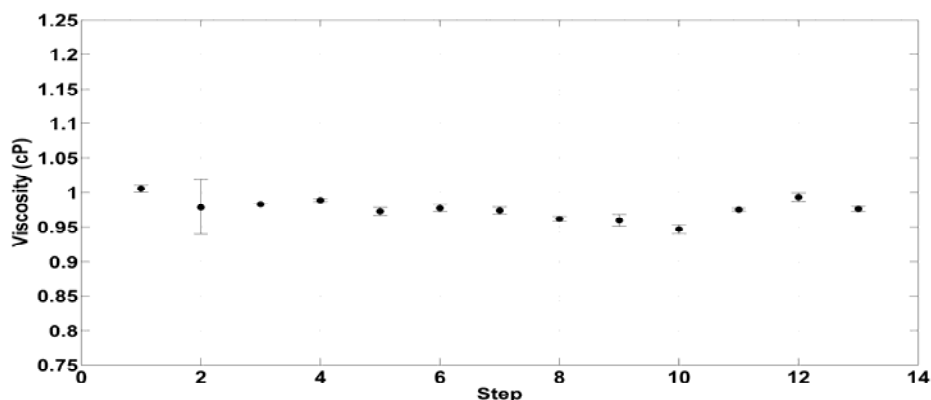
Figure 5. Viscosity During μ_a Variation

Viscosity as averaged from three samples corresponding to each step, depicted as means ± SD's (as error bars), during μ_a variation. Small variations can be seen within steps attributable to variations in sample measurements. Viscosity during step 2 has larger variations than other steps for reasons unknown, but is possibly due to operational error. The variation in viscosity across all steps is relatively low indicating stability of this parameter.
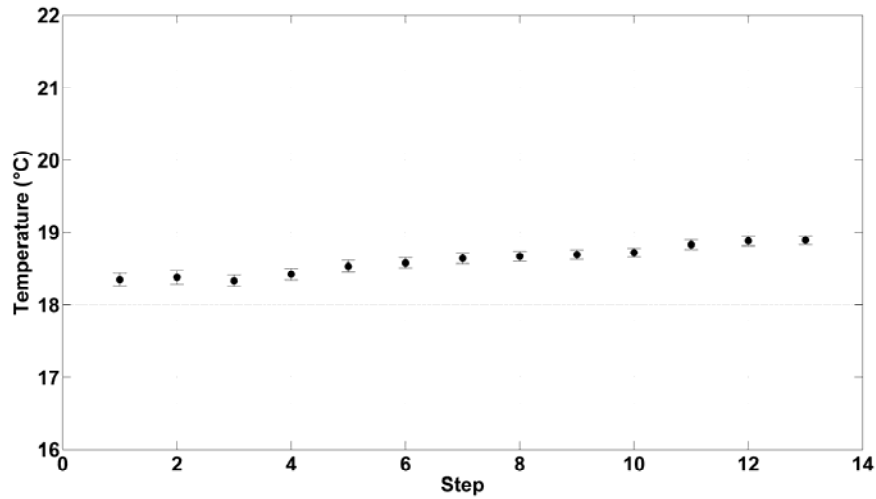
Figure 6. Temperature During μ_a Variation

Temperature as averaged over 5-minute intervals, depicted as means ± SD's (as error bars), during μ_a variation. Temperature variations within each step are small. An increasing trend is apparent and most likely the result of increasing ambient temperature within the confined room during measurements. The overall variation is small and the parameter is considered stable.
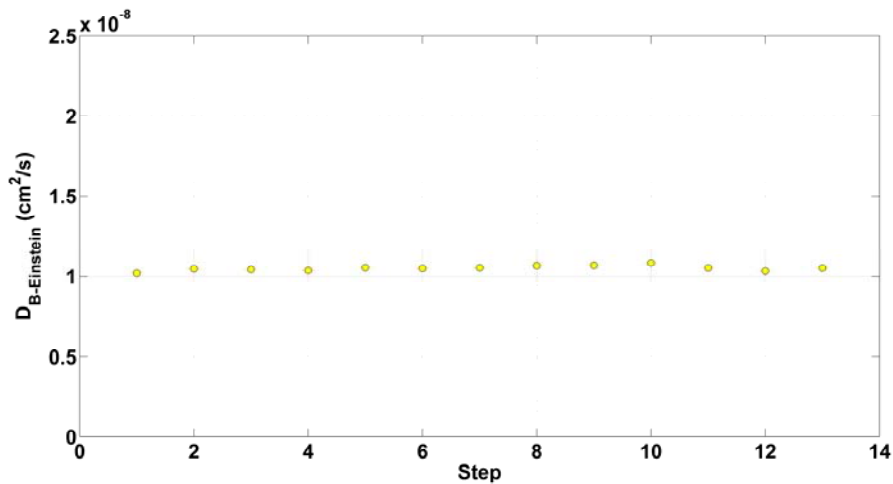
Figure 7. Brownian Motion During μ_a Variation

Stability of particle Brownian motion, with $D_{B\text{-Einstein}}$ for corresponding 5-minute intervals, during μ_a variation. The stability of this variable is exhibited with only minor variations. These fluctuations are due to the small viscosity and temperature variations governed by Eq. 7.
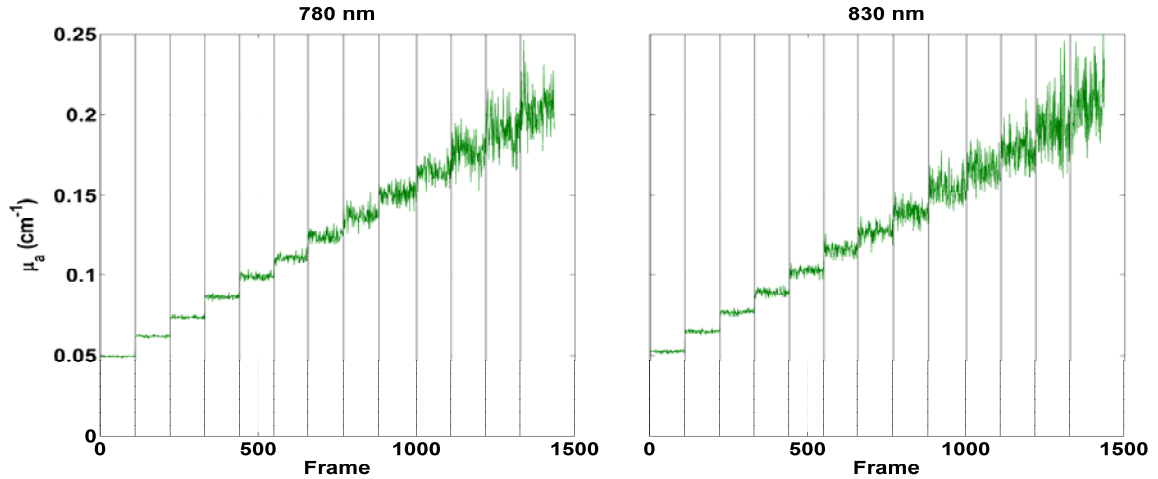
Figure 8. Raw Data of Imagent Measured μ$_a$ at 780 and 830 nm During μ$_a$ Variation

Imagent measured μ$_a$ at 780 nm (left) and 830 nm (right) acquired from each data acquisition cycle (frame) during μ$_a$ variation. The noise is relatively low at early intervals, but increases significantly near higher μ$_a$ with decreases in Imagent detected intensity.
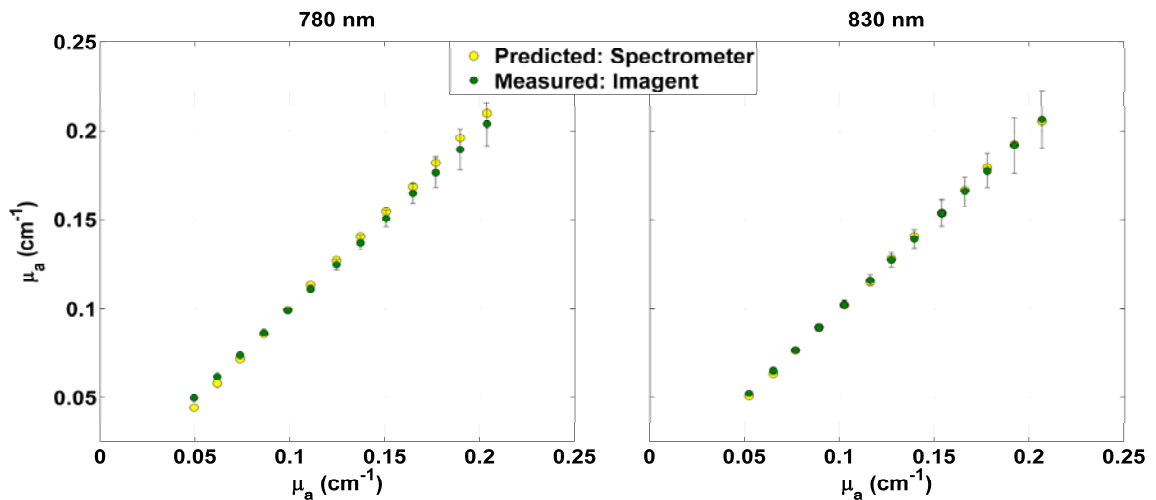
Figure 9. μ$_a$ at 780 and 830 nm During μ$_a$ Variation

Imagent measured μ$_a$, shown as interval means ± SD's, and μ$_a$ predicted using spectrometer measurements at 780 nm (left) and 830 nm (right) for μ$_a$ variation. Increases in Imagent measured μ$_a$ are in agreement with spectrometer predictions. The agreement is better at 830 nm which may be due to the detection accuracy of Imagent at separate wavelengths. Measurement variations within intervals can be seen to increase with the increasing noise shown in **Fig. 8**.
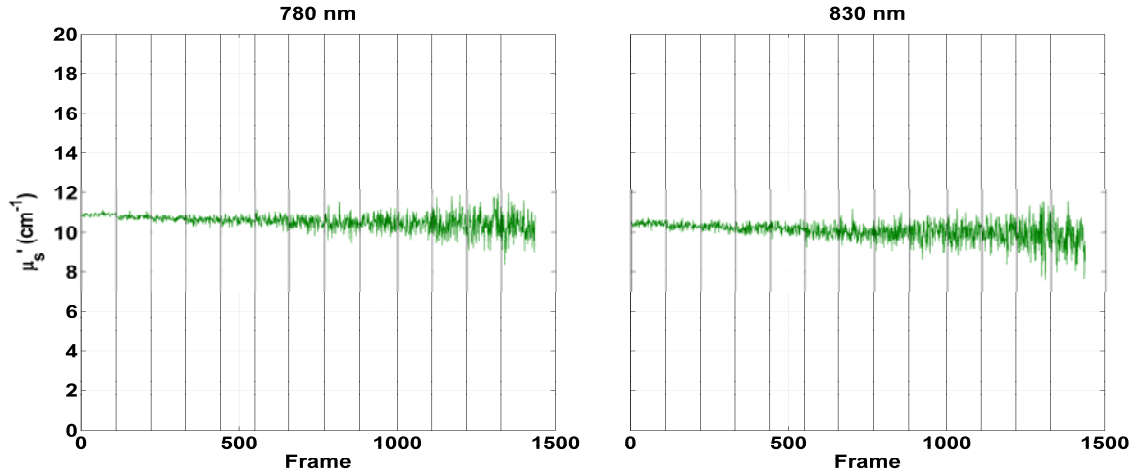
Figure 10. Raw Data of Imagent Measured μ_s' at 780 and 830 nm During μ_a Variation

Imagent measured μ_s' at 780 nm (left) and 830 nm (right) acquired from each data acquisition cycle (frame) during μ_a variation. The noise is low at early intervals and continually increases with the addition of ink at each step as Imagent detected intensity decreases. The μ_s' at both wavelengths are relatively stable throughout the measurement.
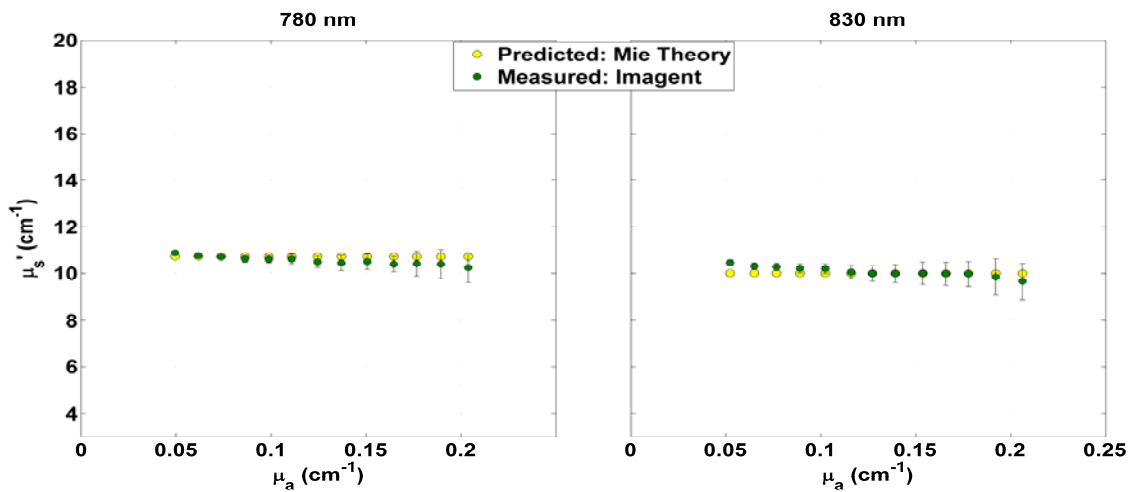
**Figure 11. μ_s' at 780 and 830 nm During μ_a Variation**

Imagent measured μ_s', shown as interval means ± SD's, and μ_s' predicted from Mie theory approximations at 780 nm (left) and 830 nm (right) for μ_a variation. Small deviations between Imagent measured μ_s' and Mie theory predictions can be seen, but are within expectations (see Chapters 3.3 and 4.2). Measurement variations within intervals can be seen to increase with the increasing noise shown in **Fig. 10**.
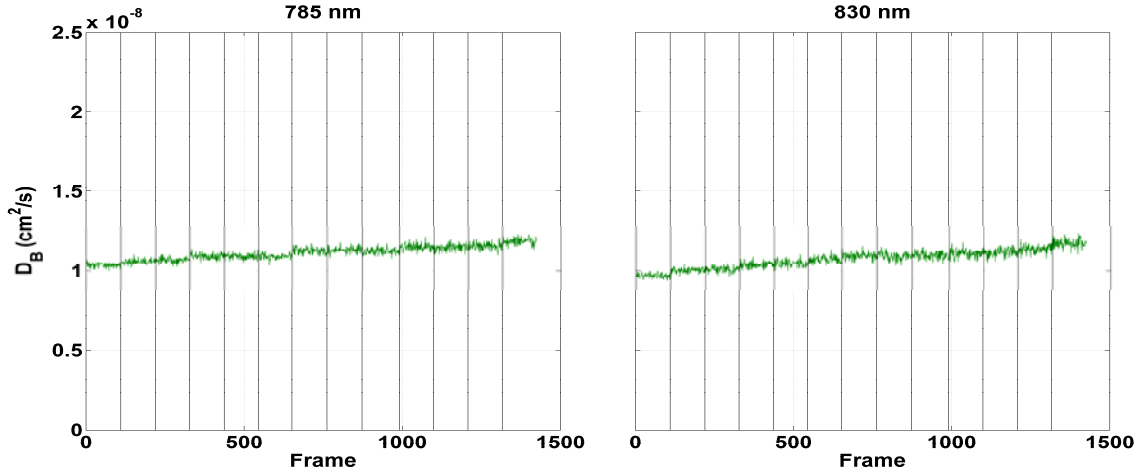
Figure 12. Raw Data of DCS Measured $D_{B\text{-dynamic}}$ at 785 and 830 nm During μ_a Variation

DCS measured $D_{B\text{-dynamic}}$ at 785 nm (left) and 830 nm (right) acquired from each data acquisition cycle (frame) during μ_a variation. Noise levels after averaging from four detectors is low for all intervals. A slightly increasing trend may be due to the decreases in diffusion applicability from increasing μ_a compared to μ_s'.
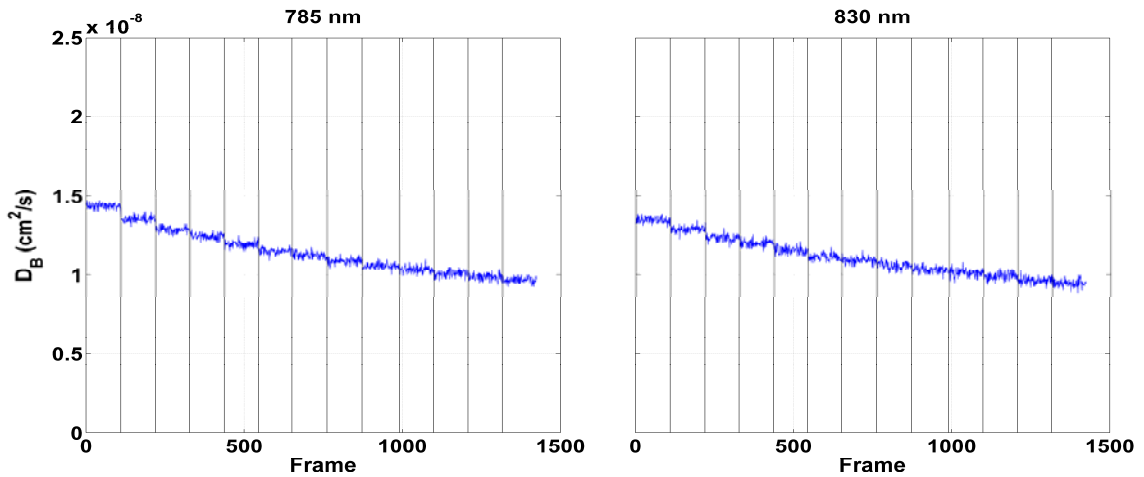
Figure 13. Raw Data of DCS Measured $D_{B\text{-mid}}$ at 785 and 830 nm During μ_a Variation

DCS measured $D_{B\text{-mid}}$ at 785 nm (left) and 830 nm (right) acquired from each data acquisition cycle (frame) during μ_a variation. Noise levels after averaging from four detectors is low for all intervals, the same as for $D_{B\text{-dynamic}}$ (see **Fig. 12**). The largely decreasing trend is expected to be due to the lack of accounting for changes in the optical properties.
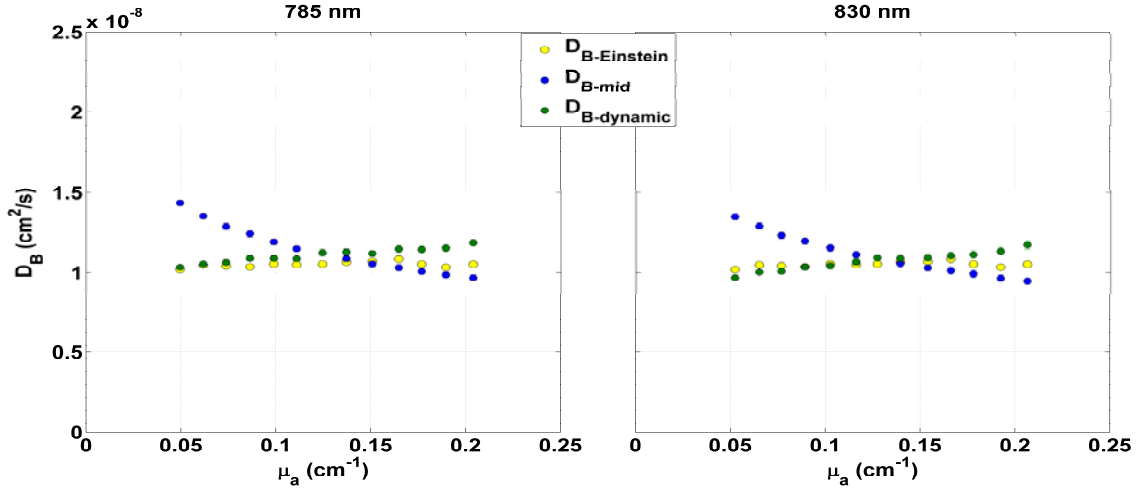
Figure 14. D_B at 785 and 830 nm During μ_a Variation

DCS $D_{B\text{-dynamic}}$ and $D_{B\text{-mid}}$, shown as interval means ± SD's, and Brownian diffusion coefficients, $D_{B\text{-Einstein}}$, at 785 nm (left) and 830 nm (right) for μ_a variation. This figure overlays the $D_{B\text{-Einstein}}$ from **Fig. 7** with the interval means of DCS measured $D_{B\text{-mid}}$ and $D_{B\text{-dynamic}}$ from **Fig. 12** and **13**. Deviations between $D_{B\text{-mid}}$ appear to be much greater than $D_{B\text{-dynamic}}$ in comparison to $D_{B\text{-Einstein}}$ (true flow index) indicating $D_{B\text{-dynamic}}$ as the more accurate flow index.

3.2 μ_s' Variation

Results of the μ_s' variation experiment are given in the same format as that for μ_a variation. Thirteen steps of increasing μ_s' were carried out with a step size of 1 cm^{-1} covering μ_s' (830 nm) from 4 to 16 cm^{-1} with constant μ_a (830 nm) = 0.125 cm^{-1}. The viscosity, temperature, and calculated $D_{B\text{-Einstein}}$ means with SD's as error bars are displayed in **Fig. 15 – 17**, respectively. Note that the same $D_{B\text{-Einstein}}$ set is used as the true flow indices for comparison with both DCS source wavelengths. Raw data and interval means of measured μ_a, μ_s', $D_{B\text{-Einstein}}$, $D_{B\text{-dynamic}}$, and $D_{B\text{-mid}}$ with SD error bars are shown in **Fig. 18 – 24** along with predicted μ_a and μ_s' (as done in Chapter 3.1). Raw data figures (**Fig. 18**, **20**, **22**, and **23**) are presented in a similar fashion to Chapter 3.1.
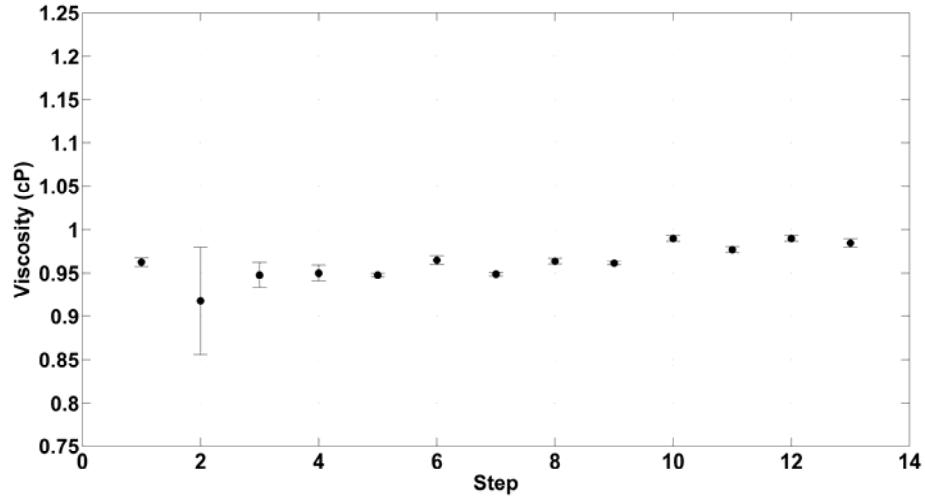
Figure 15. Viscosity During μ$_s$' Variation

Viscosity as averaged from three samples corresponding to each step, depicted as means ± SD's (as error bars), during μ$_s$' variation. These measurements exhibit small variations within steps due to sample variations, but are stable overall. Step 2 has larger variations for reasons possibly due to operational error.
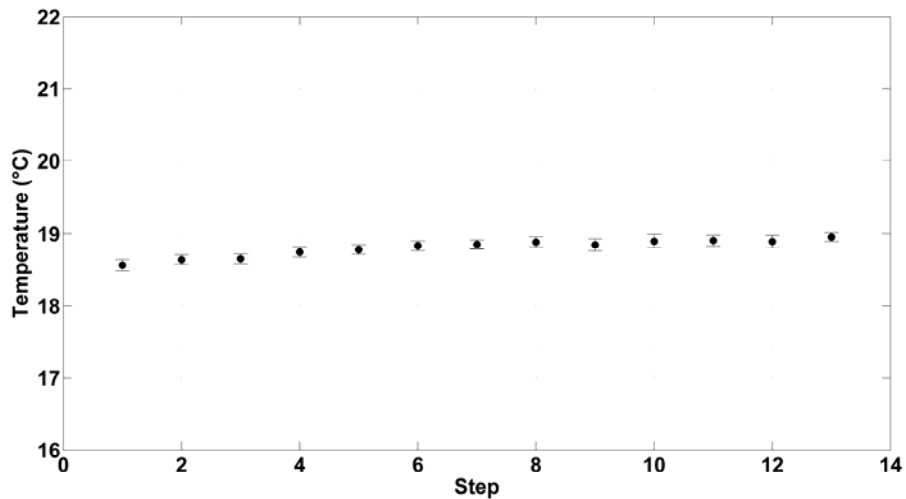
Figure 16. Temperature During μ$_s$' Variation

Temperature is averaged over 5-minute intervals, depicted as means ± SD's (as error bars), during μ$_s$' variation. Temperature variations within each step are small, but overall stable with a generally increasing trend caused from increases in ambient temperature within the confined room throughout measurements.
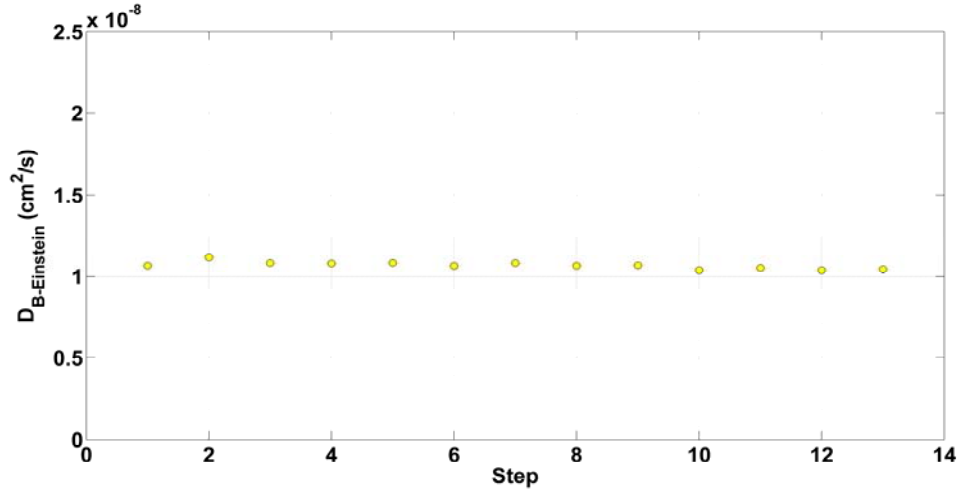
Figure 17. Brownian Motion During μ$_s$' Variation

Stability of particle Brownian motion, with D$_{B\text{-Einstein}}$ for corresponding 5-minute intervals, during μ$_s$' variation. This variable shows as stable with only minor variations caused by small viscosity and temperature variations governed by Eq. 7.
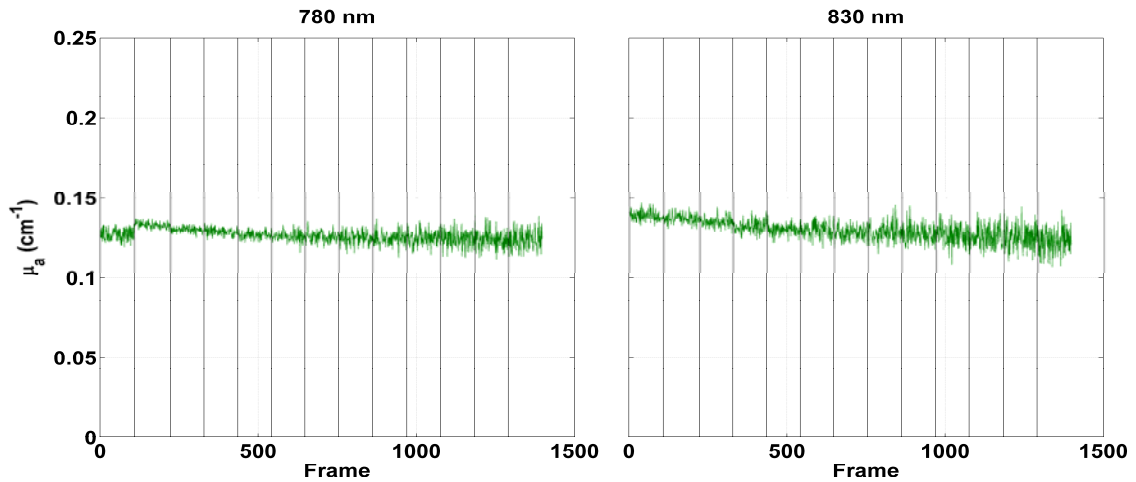
Figure 18. Raw Data of Imagent Measured μ$_a$ at 780 and 830 nm During μ$_s$' Variation

Imagent measured μ$_a$ at 780 nm (left) and 830 nm (right) acquired from each data acquisition cycle (frame) during μ$_s$' variation. The noise is slightly higher than during μ$_a$ variation at early intervals, likely due to the high Intralipid concentration, increasingly worsening throughout the measurement. The μ$_a$ is relatively stable overall with a small jump occurring from the first and second intervals at 780 nm. This jump may be caused by near saturation of the Imagent detectors at the earliest interval.
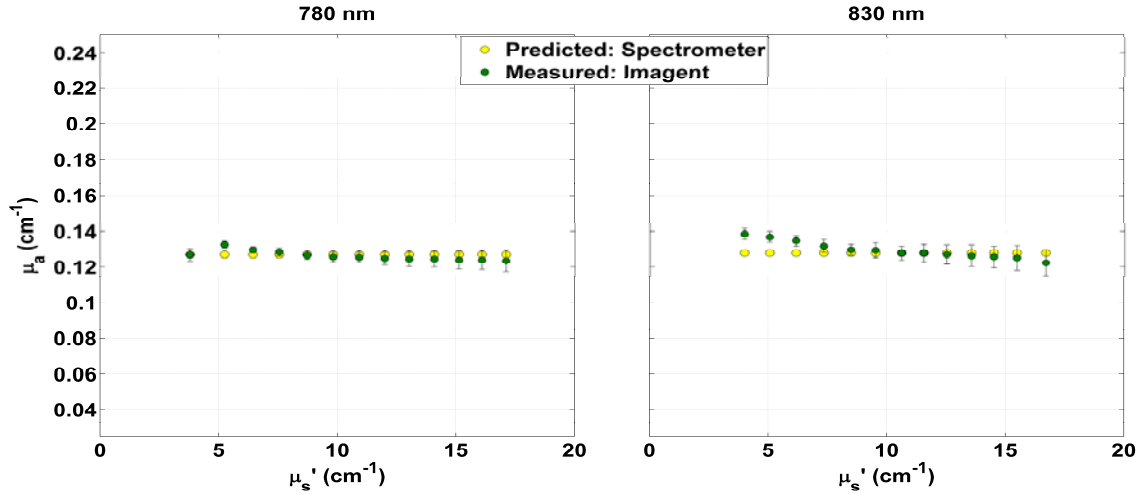
Figure 19. μ_a at 780 and 830 nm During μ_s' Variation

Imagent measured μ_a, shown as interval means ± SD's, and μ_a predicted using spectrometer measurements at 780 nm (left) and 830 nm (right) for μ_s' variation. The deviations between Imagent measured μ_s' and Mie theory predictions are minor, but within expectations (see Chapters 3.3 and 4.2). Measurement variations within intervals can be seen to increase with the increasing noise shown in **Fig. 18**.
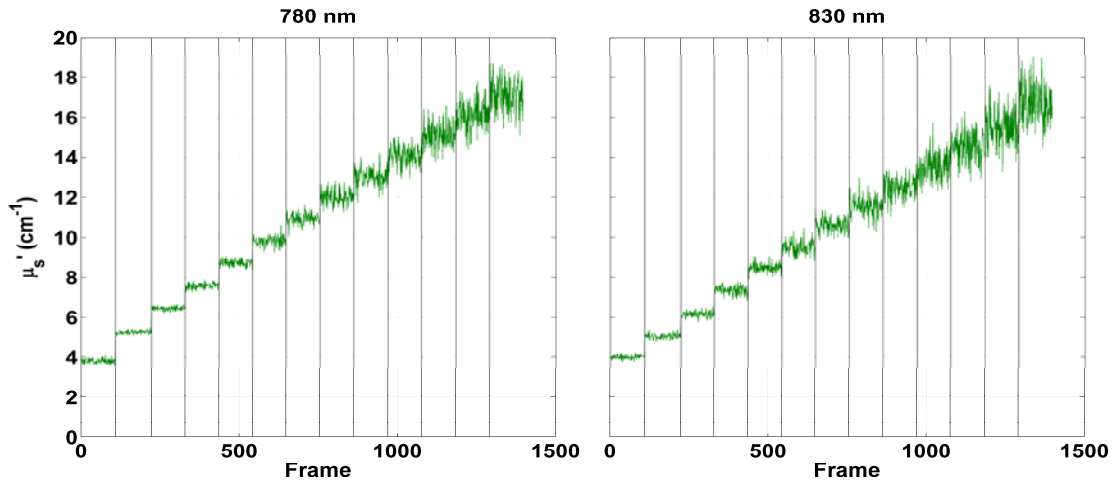
Figure 20. Raw Data of Imagent Measured μ_s' at 780 and 830 nm During μ_s' Variation

Imagent measured μ_s' at 780 nm (left) and 830 nm (right) acquired from each data acquisition cycle (frame) during μ_s' variation. Noise is low early and increases with each step and the addition of Intralipid which decreases the Imagent detected intensity.
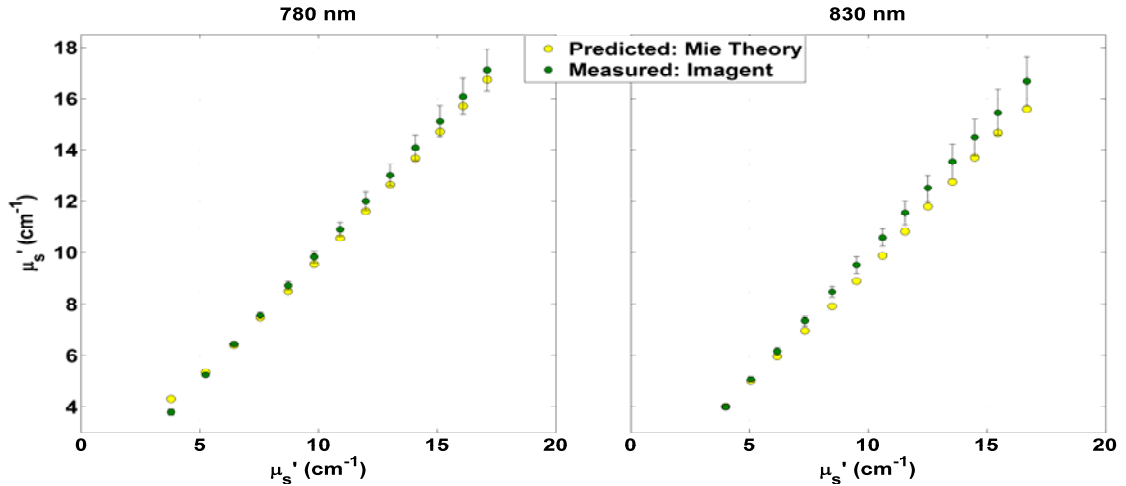
Figure 21. μ_s' at 780 and 830 nm During μ_s' Variation

Imagent measured μ_s', shown as interval means ± SD's, and μ_s' predicted from Mie theory approximations at 780 nm (left) and 830 nm (right) for μ_s' variation. Increases in Imagent measured μ_s' are in agreement with Mie theory predictions. The agreement at 780 nm appears better which may be due to the detection accuracy of Imagent at separate wavelengths, similar to μ_a during μ_a variation (see **Fig. 9**). Measurement variations within intervals can be seen to increase with the increasing noise shown in **Fig. 20**.
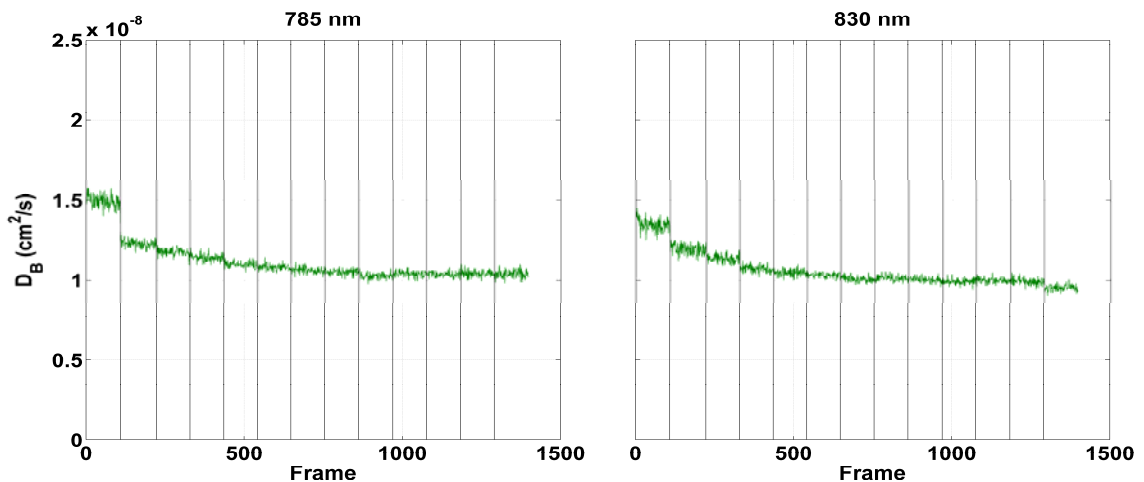
Figure 22. Raw Data of DCS Measured $D_{B\text{-dynamic}}$ at 785 and 830 nm During μ_s' Variation

DCS measured $D_{B\text{-dynamic}}$ at 785 nm (left) and 830 nm (right) acquired from each data acquisition cycle (frame) during μ_s' variation. Noise levels are low for all intervals with detector averaging. The trend is decreasing at early intervals before stabilizing around the fourth and fifth intervals. This is possibly due to poor diffusion from a low μ_s' compared to μ_a.
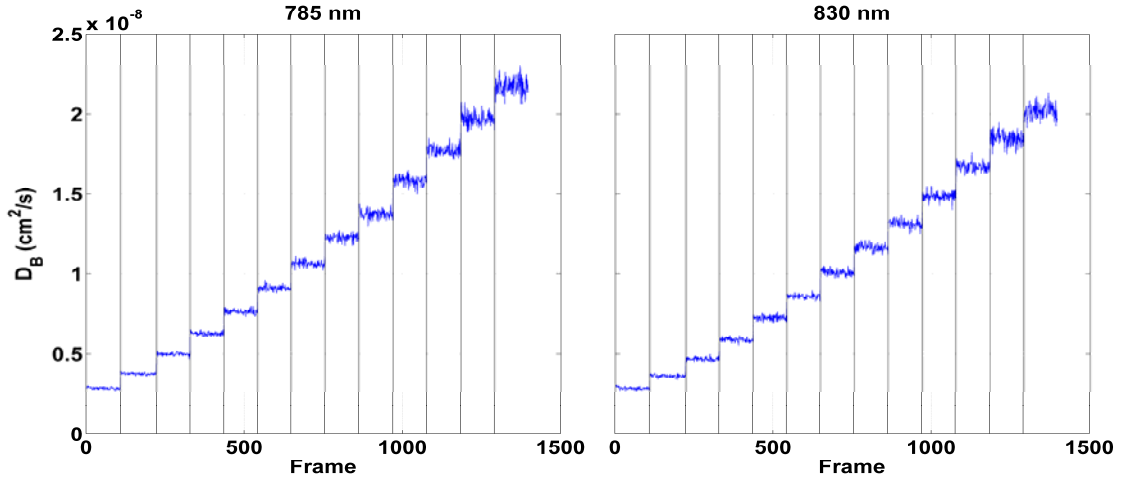
Figure 23. Raw Data of DCS Measured $D_{B\text{-mid}}$ at 785 and 830 nm During μ_s' Variation

DCS measured $D_{B\text{-mid}}$ at 785 nm (left) and 830 nm (right) acquired from each data acquisition cycle (frame) during μ_s' variation. Noise levels are low as was the case for $D_{B\text{-dynamic}}$ (see **Fig. 22**). There is a largely increasing trend due to the lack of accounting for changes in the optical properties.
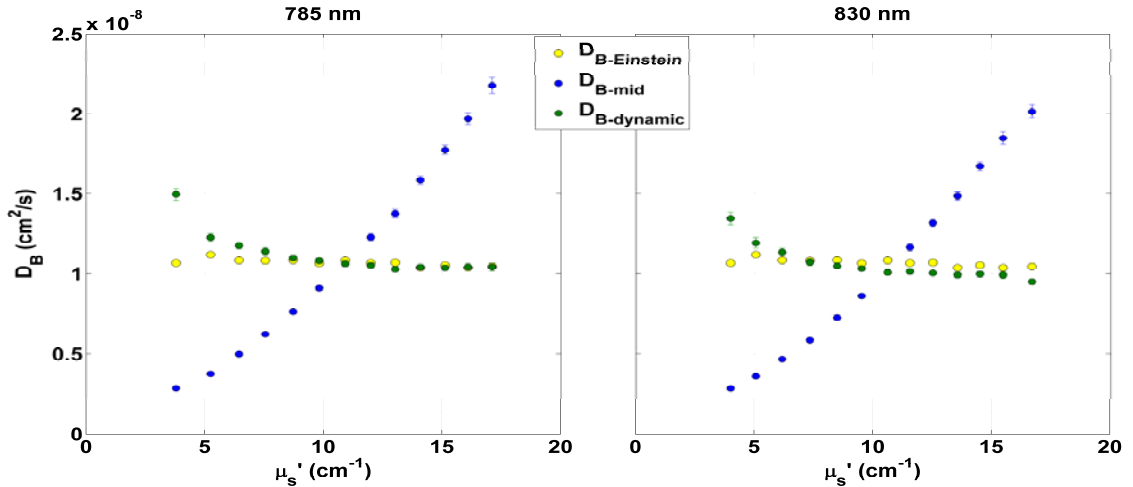
Figure 24. D_B at 785 and 830 nm During μ_s' Variation

DCS $D_{B\text{-dynamic}}$ and $D_{B\text{-mid}}$, shown as intervals means ± SD's, and Brownian diffusion coefficients, $D_{B\text{-Einstein}}$, at 785 nm (left) and 830 nm (right) for μ_s' variation. As was done for μ_a variation, this figure overlays the $D_{B\text{-Einstein}}$ from **Fig. 17** with the interval means of DCS measured $D_{B\text{-mid}}$ and $D_{B\text{-dynamic}}$ from **Fig. 22** and **23**. Deviations between $D_{B\text{-mid}}$ are significantly greater than $D_{B\text{-dynamic}}$ in comparison to $D_{B\text{-Einstein}}$ (true flow index) indicating $D_{B\text{-dynamic}}$ as the more accurate flow index.

40

3.3 Quantification of μ_a and μ_s' Influences on Flow Indices

Influence of μ_a and μ_s' variations on $D_{B\text{-Einstein}}$. Variations in phantom optical properties are examined to determine any potential influences on $D_{B\text{-Einstein}}$. Using the data displayed in **Fig. 5 – 7** and **15 - 17**, the means, SD's, and coefficients of variation (CV) were calculated over the entire μ_a and μ_s' variation experiments for viscosity, temperature, and $D_{B\text{-Einstein}}$. The results are shown in Table 1, with experiments separated into different columns. No major influences are noticeable on $D_{B\text{-Einstein}}$ or related parameters with CV's less than 2.2% for all three in both optical property variations. With this knowledge, the $D_{B\text{-Einstein}}$ is considered viable as the true flow index for determining measurement errors in DCS flow indices.

Table 1. Mean ± Standard Deviation and Coefficients of Variation of Viscosity, Temperature, and Brownian Motion

Variables	μ_a variation		μ_s' variation	
	Mean ± SD	CV	Mean ± SD	CV
Viscosity (cP)	0.98 ± 0.02	1.54%	0.96 ± 0.02	2.12%
Temperature (°C)	18.61 ± 0.20	1.05%	18.80 ± 0.12	0.64%
$D_{B\text{-Einstein}}$ (cm^2/s)	1.05E-08 ± 1.65E-10	1.57%	1.07E-08 ± 2.25E-10	2.11%

Mean measurement errors in μ_a, μ_s' and DCS flow indices. Measurements errors are described using absolute percentage errors defined as:

$$\text{Absolute Percentage Error} = \frac{|\text{Estimate} - \text{True}|}{\text{True}} \times 100\% \tag{13}$$

41

In the case of DCS flow indices, $D_{B\text{-Einstein}}$ is considered the true flow index whereas $D_{B\text{-dynamic}}$ and $D_{B\text{-mid}}$ are estimates. Estimated μ_a and μ_s' are those averaged from measurements while true values are from spectrometer and Mie theory predictions, respectively. Using the estimated and true data (shown in **Fig. 9**, **11**, **14**, **19**, **21**, and **24**) over the complete range of μ_a and μ_s' variations, measurement errors were calculated and their means ± SD's are shown in Table 2. P-values are also shown for 2-sample unequal variance, two-tailed Student t-tests between mean measurement errors at the wavelengths used. Significant differences are denoted with a * prefix when p-values are less than 0.05. Measurement errors for μ_a and μ_s' are less than 6% for both experiments and sets of wavelengths. DCS flow indices, however, exhibit some discrepancies amongst their measurement errors. Errors in $D_{B\text{-mid}}$ are overall higher than those of $D_{B\text{-dynamic}}$, indicating optical properties influence in DCS D_B calculations. Variations in μ_s' appear to contribute a greater influence on flow index errors than μ_a variations, as identified by $D_{B\text{-mid}}$ errors up to 12.89% during μ_a variation and 49.63% during μ_s' variation. Student t-test results identified significant differences between mean measurement errors at 780 and 830 nm for μ_a during μ_a variation (p = 0.01) and μ_s' during μ_s' variation (p = 0.04). Detection accuracy of the Imagent at the different wavelengths is thought to be the greatest attributor to these differences. No other significant differences were found between the mean measurement errors at both wavelengths.

Table 2. Imagent/DCS Measurement Percentage Errors at 780/785 nm (shaded) and 830/830 nm

(non-shaded)

Variables		μ_a variation (Absolute % Error)		μ_s' variation (Absolute % Error)	
		Mean ± SD	p-value	Mean ± SD	p-value
μ_a	780 nm	3.39 ± 3.07	*0.01	1.86 ± 1.15	0.23
	830 nm	0.84 ± 0.95		2.86 ± 2.69	
μ_s'	780 nm	1.93 ± 1.23	0.54	3.14 ± 2.66	*0.04
	830 nm	1.60 ± 1.50		5.29 ± 2.27	
$D_{B\text{-dynamic}}$	785 nm	5.52 ± 3.69	0.28	5.84 ± 10.73	0.83
	830 nm	4.02 ± 3.30		6.58 ± 6.16	
$D_{B\text{-mid}}$	785 nm	12.89 ± 12.00	0.64	49.63 ± 31.51	0.81
	830 nm	10.89 ± 8.99		46.76 ± 27.44	

* p-values < 0.05

For both experiments, Student t-tests were also used for comparisons between the mean measurement errors of $D_{B\text{-mid}}$ and $D_{B\text{-dynamic}}$, within the same wavelengths, as shown in Table 3. Significant differences are determined and noted similarly as done in Table 2. It is readily seen that $D_{B\text{-mid}}$ and $D_{B\text{-dynamic}}$ are not equivalent by the significant (although for 785 nm during μ_a variation it is borderline) differences found for both wavelengths and experiments. Additionally, $D_{B\text{-dynamic}}$ is considered more accurate as it provides less measurement errors (see Table 2). As similarly suggested from Table 2, the μ_s' influence on DCS flow indices is greater than μ_a as indicated by much lower p-values during μ_s' variation.

Table 3. P-values for Comparisons of the Mean Measurement Errors Between DCS Flow Indices Calculated with Dynamic Vs. Assumed Constant Optical Properties

$D_{B\text{-dynamic}}$ vs. $D_{B\text{-mid}}$	μ_a variation (p-value)	μ_s' variation (p-value)
785 nm	0.0525	*0.0003
830 nm	*0.0205	*0.0002

* p-values < 0.05

Influence of μ_a and μ_s' variations on DCS flow index. Percentage errors (not absolute) are used to visualize the influences of the individual optical properties on flow indices, defined by the following equations:

$$\% \ \text{Error} \ \mu_a = \frac{\mu_{a-\text{mid}} - \mu_{a-\text{dynamic}}}{\mu_{a-\text{dynamic}}} \times 100\% \tag{14}$$

$$\% \ \text{Error} \ \mu_s' = \frac{\mu_s'_{-\text{mid}} - \mu_s'_{-\text{dynamic}}}{\mu_s'_{-\text{dynamic}}} \times 100\% \tag{15}$$

$$\% \ \text{Error} \ D_B = \frac{D_{B-\text{mid}} - D_{B-\text{dynamic}}}{D_{B-\text{dynamic}}} \times 100\% \tag{16}$$

The estimates for these errors are the assumed optical properties (middle-interval) and subsequent $D_{B\text{-mid}}$ per interval. The true values are the averaged optical properties measured by Imagent (dynamic) and subsequent $D_{B\text{-dynamic}}$ per interval. Resulting percentage errors in DCS D_B due to inaccurate estimations of optical properties are overlaid for both wavelengths and experiments in **Fig. 25**. Note that errors in μ_a are during μ_a variation and those in μ_s' during μ_s' variation. In agreement with results thus far the μ_s' shows a larger influence on DCS flow indices, as visible by the wider range of D_B percentage errors, than μ_a. The trends in errors for μ_a and μ_s' with those in D_B also differ. Overestimation and underestimation of μ_a result in overestimation and underestimation in

DCS D_B. On the contrary, μ_s' overestimation and underestimation lead to D_B underestimation and overestimation. Both wavelengths display analogous behavior and are in good agreement.
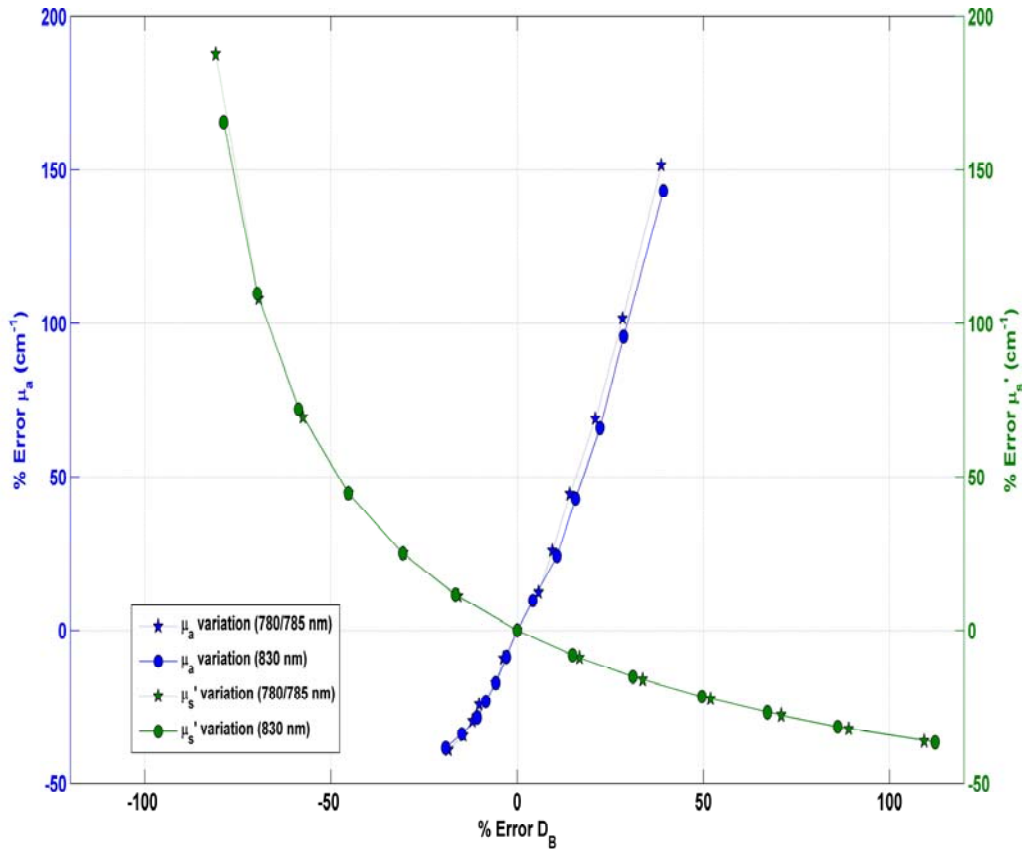
Figure 25. DCS Flow Index Errors Due to Inaccurate Optical Property Estimations

Inaccurate estimations (percentage errors) of μ_a and μ_s' result in corresponding percentage D_B errors between $D_{B\text{-dynamic}}$ and $D_{B\text{-mid}}$ for both wavelengths.

3.4 Influence of Tissue Optical Properties on Head/Neck Tumor Blood Flow Index

Ten patients with head and neck tumors, measured for hemodynamic information, have their DCS flow indices evaluated for optical property influences. The resulting mean optical properties over patients are: μ_a (830 nm) = 0.12 ± 0.03 cm^{-1} and μ_s' (830 nm) = 7.80 ± 2.64 cm^{-1}. The means $\pm$ SD's (error bars) of tumor μ_a and μ_s' are shown in **Fig. 26** and **27**, respectively. Red and blue dots denote the overall patient maximum and minimum optical properties, respectively. Patient blood flow indices ($\alpha D_{B\text{-dynamic}}$, $\alpha D_{B\text{-min}}$, $\alpha D_{B\text{-mean}}$, and $\alpha D_{B\text{-max}}$) along with percentage errors thereof (aside from $\alpha D_{B\text{-dynamic}}$) are given in **Fig. 28** and **29**. Note that the assumption of $\alpha = 1$ from phantom experiments is no longer correct as the real tissue consists of both static and dynamic scatterers. Diffusion coefficient percentage errors are calculated using Eq. 16 by replacing the phantom study estimate, $D_{B\text{-mid}}$, with the corresponding tumor study estimates $\alpha D_{B\text{-min}}$, $\alpha D_{B\text{-mean}}$, and $\alpha D_{B\text{-max}}$. Also, the true flow index $D_{B\text{-dynamic}}$, calculated using Imagent measured optical properties, from the phantom study is replaced in Eq. 16 by the equivalent tumor study true flow index, $\alpha D_{B\text{-dynamic}}$. This produces percentage errors for each flow index estimate for each patient (see **Fig. 29**).
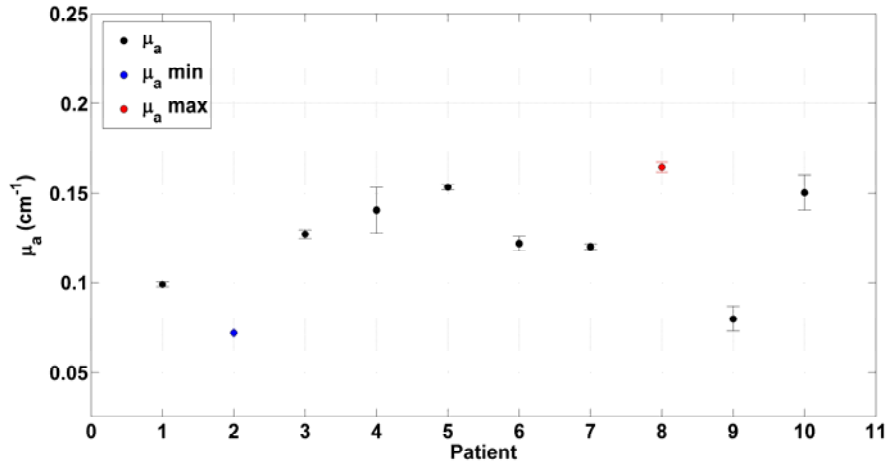
Figure 26. Tumor μ_a at 830 nm

Imagent measured μ_a, shown as means ± SD's, obtained at 830 nm from tumor region for 10 subjects with head and neck tumors during tumor study. Large variations can be seen to exist between the 10 subjects.
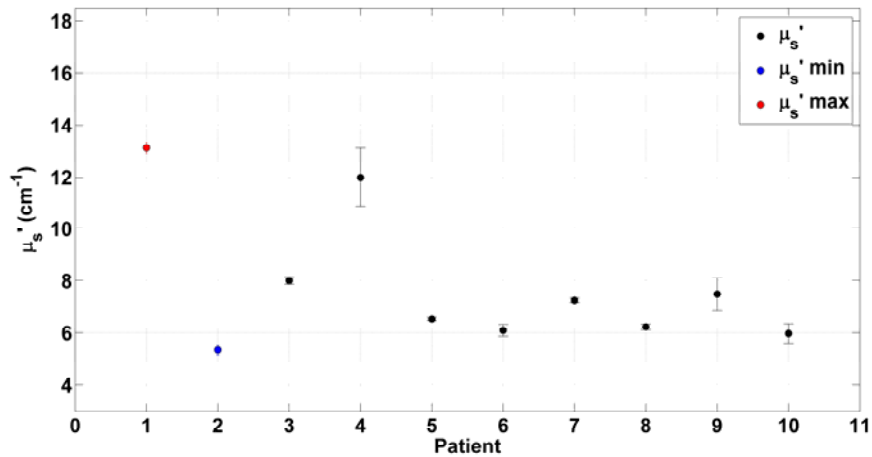
Figure 27. Tumor μ_s' at 830 nm

Imagent measured μ_s', shown as means ± SD's, obtained at 830 nm from tumor region for 10 subjects with head and neck tumors during tumor study. Similar to μ_a in **Fig. 26**, large variations also exist in μ_s' between the 10 subjects.
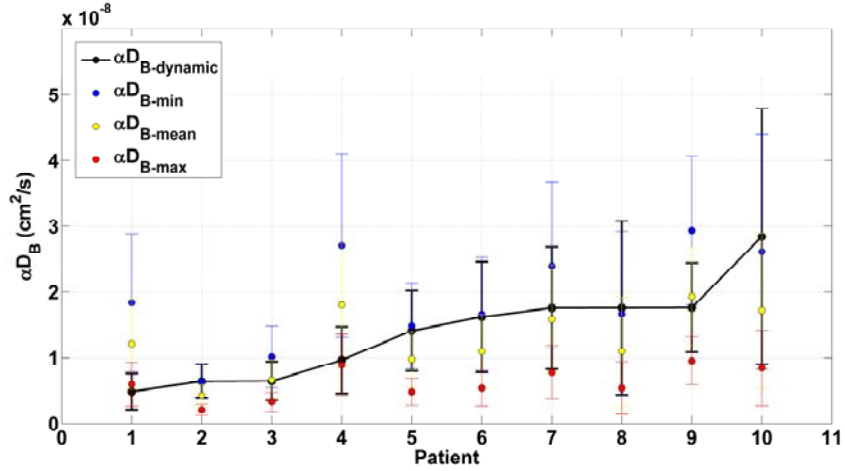
Figure 28. Tumor Flow Indices at 854 nm

DCS flow indices measured by DCS, shown as means ± SD's, obtained at 854 nm from tumor region for 10 subjects with head and neck tumors and calculated using 830 nm optical properties during tumor study. Patients are listed in order of increasing $\alpha D_{B\text{-dynamic}}$ (854 nm). The underestimation of optical properties ($\alpha D_{B\text{-min}}$) overestimates the flow indices whereas overestimating optical properties ($\alpha D_{B\text{-max}}$) underestimates flow indices. These trends agree with phantom study results of a larger influence from μ_s'.
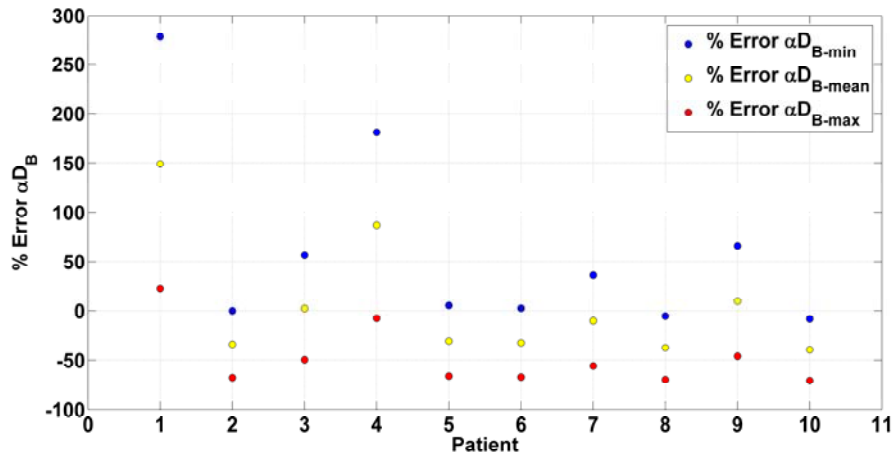
Figure 29. Tumor Flow Index Errors

Percentage errors in DCS flow indices at 854 nm from tumor region for 10 subjects with head and neck tumors. DCS flow indices $\alpha D_{B\text{-min}}$, $\alpha D_{B\text{-mean}}$, and $\alpha D_{B\text{-max}}$ are considered estimates with $\alpha D_{B\text{-dynamic}}$ as true flow indices for patients. The errors are shown to increase substantially with inaccuracies in optical properties (see **Fig. 26** and **27**).

To ease identification of differences in patient DCS flow index trends using the diverse optical properties sets, they are ordered by increasing $\alpha D_{B\text{-dynamic}}$ (true flow index). A black line denotes the true flow indices data. Note that the patient numbers depicted represent indices for trend illustration and are not related to those corresponding to the actual measurement sequence. After this ordering, trend changes when calculating flow indices without the true optical properties can be viewed (**Fig. 28**). When the μ_a and μ_s' are inaccurately estimated ($\alpha D_{B\text{-min}}$, $\alpha D_{B\text{-mean}}$, and $\alpha D_{B\text{-max}}$), the trends do not agree with the true flow index trend ($\alpha D_{B\text{-dynamic}}$). The αD_B estimates result in a wide range of percentage errors: $\alpha D_{B\text{-min}}$ from -8.07 to 278.15%, $\alpha D_{B\text{-mean}}$ from -39.48 to 149.01%, and $\alpha D_{B\text{-max}}$ from -70.26 to 22.59%. The tumor study data is consistent with expectations from phantom study results with μ_s' variation appearing to play a greater role than μ_a in DCS flow index errors. From **Fig. 28**, the consequential overestimation and underestimation of blood flow indices are opposite of those of μ_s' variation, as seen in **Fig. 25**.

CHAPTER 4: DISCUSSION AND CONCLUSIONS

This chapter begins with discussion on the influences of μ_a and μ_s' variations on $D_{B\text{-}Einstein}$ (Chapter 4.1). Findings related to measurement errors in μ_a, μ_s' and $D_{B\text{-}dynamic}$ are then examined (Chapter 4.2). Next, the flow index errors due to the assumption of optical properties are discussed (Chapter 4.3). A comparison is then provided between the *in-vivo* tumor study data and phantom study results (Chapter 4.4). Finally, conclusions from this study are given (Chapter 4.5).

4.1 μ_a and μ_s' Variation Influences on $D_{B\text{-}Einstein}$

The Brownian motion of spherical particles, $D_{B\text{-}Einstein}$, from the Intralipid solution in liquid phantoms is calculated from the Einstein-Stokes formula (Eq. 7). This movement is calculated based on the liquid phantom temperature, spherical particle radius, and viscosity. The temperature has only small variations during both phantom experiments (see Table 1, **Fig. 6**, and **Fig. 16**), with CV < 1.1%. Due to the ~4.5 hour duration of each experiment, a general increase in ambient and thus phantom temperature is expected. This increase includes heat from running equipment within the small, confined room. The particle radius is assumed to be relatively constant during both experiments, with Intralipid provided from the same batch supply. Only minor variations in viscosity are evident, with CV < 2.2% for both experiments (see Table 1, **Fig. 5**, and **Fig. 15**). These variations may be the result of the viscometer sensitivity at measurements near the bottom of its range (0.2 cP) and minor sample-to-sample variations. The Newtonian fluid assumption is determined acceptable as the samples measured at three separate RPMs

showed small variation. Because of the stability of viscosity and temperature measurements as well as the assumed constant particle radius, $D_{B\text{-Einstein}}$ is also expected to be constant. This is found to be the case as is seen in **Fig. 7** and **17** and with CV < 2.2% for $D_{B\text{-Einstein}}$ from Table 1.

The addition of ink and Intralipid solutions during μ_a and μ_s' variation, respectively, are not parameters expected to contribute to variations in $D_{B\text{-Einstein}}$. Ink solution should have no particles undergoing Brownian motion. On the other hand, Intralipid solution does contain particles undergoing Brownian motion, but this motion is not anticipated to change during measurement. Additions of Intralipid provide more scatterers undergoing Brownian motion, but the particle motion is equivalent for all. The ratio of moving to total scatterers (α) should also remain unchanged ($\alpha = 1$) given that only the dynamic particles from Intralipid are scatterers. The viscosity of ink and Intralipid solution is, as mentioned, primarily water and variations thereof should not result in changing the phantom viscosity. Similarly, the ink and Intralipid solutions were at room temperature at the time of the experiments, just as the liquid phantom, having little influence on temperature variations. From **Fig. 5-7**, **9**, **15-17**, and **21** the liquid phantom optical properties exhibit independence from viscosity, temperature and $D_{B\text{-Einstein}}$. With the optical property independence and $D_{B\text{-Einstein}}$ stability, it is therefore considered reasonable to use as the true flow index for liquid phantom spherical particle motion.

4.2 Measurement Errors of μ_a, μ_s', and $D_{B\text{-dynamic}}$

From **Fig. 9**, **11**, **19**, and **21** the utilization of ink and Intralipid solutions for manipulating μ_a and μ_s', respectively, is validated. The incremental addition of ink solution results in a linear increase in measured μ_a with relative stability of μ_s' at both wavelengths, as expected. Similarly, Intralipid solution linearly increases only μ_s' at both wavelengths. These measured optical properties were also found to be in good agreement with the spectrometer and Mie theory predictions. Variation patterns in Imagent optical property measurements may have been influenced by calibration at the midpoint: μ_a (830 nm) = 0.125 cm^{-1}, μ_s' (830 nm) = 10 cm^{-1}.

Measurement errors in μ_s' were less than 6% (see Table 2) for both wavelengths and experiments comparable to the literature using Mie theory estimation (see Chapter 2.7) [61]. Overall, average measurement errors for μ_a/μ_s' are minimal with less than 4%/6% during μ_a/μ_s' variations. Previous studies experienced measurement error levels in this range as well using frequency-domain spatially resolved NIRS [47, 48]. In comparing optical property measurement errors at 780 and 830 nm, significant differences were determined for μ_a during μ_a variation and μ_s' during μ_s' variation. The detection accuracy of the Imagent at separate wavelengths is most likely the cause of such significance. No significant differences were found between $D_{B\text{-dynamic}}$ measurement errors at 785 and 830 nm. These $D_{B\text{-dynamic}}$ errors averaged less than 7%, comparable to those of optical properties (less than 6%), for both wavelengths and experiments. This likeness implies optical property influences on DCS D_B.

4.3 Resulting D_B Errors from Optical Property Assumptions

Inaccurate estimations of μ_a and μ_s' both produced higher D_B measurement errors ($D_{B\text{-mid}}$) than in comparison with the true measurements ($D_{B\text{-dynamic}}$). From Table 2, $D_{B\text{-mid}}$ errors were ~13% for μ_a variation, ~50% for μ_s' variation, and only ~7% for $D_{B\text{-dynamic}}$ in both cases. From Table 3, Student t-tests compliment this lack of resemblance between measured and true D_B by their significant differences. Comparisons between $D_{B\text{-mid}}$ errors due to the influence of μ_a and μ_s' variations further extend this conclusion to include that μ_s' is a greater contributor than μ_a. This is elicited by the higher $D_{B\text{-mid}}$ measurement errors during μ_s' variation (Table 2), great differences in calculated p-values (Table 3), and larger range of D_B percentage errors due to inaccurate estimations of μ_s' (**Fig. 25**). The phase shifts of light due to dynamic scatterers collectively induce the light speckle fluctuations. As DCS flow indices are derived from these fluctuations it is expected that errors be more exaggerated by inaccurate scattering estimations. Coupling much larger scattering over absorption (i.e., μ_s' $\gg \mu_a$) in the liquid phantoms and biological tissues with the definition of K^2 (see Eq. 3) and the $\mu_s'^2$ term further support is given to μ_s' having more significance than μ_a. Wavelengths were not determined to be a decisive parameter in D_B measurement errors due to optical property assumptions. During both experiments, no significant difference was found between $D_{B\text{-dynamic}}$ and $D_{B\text{-mid}}$ at 785 and 830 nm (Table 2) and their trends were nearly identical as seen in **Fig. 25**. Due to the closeness of the wavelengths employed, more information may be exposed by choosing a wider range.

Further disparity between the influences of μ_a and μ_s' variations on DCS flow index errors exists within their related trends (see **Fig. 14**, **24**, and **25**). Overestimated and

underestimated μ_a produces overestimated and underestimated D_B, respectively. Conversely, overestimated and underestimated μ_s' produces underestimated and overestimated D_B, respectively. By examination of the boundaries of our tested optical property inaccuracies (**Fig. 25**), the largest expected deviations in DCS flow indices can be estimated. Overestimating/underestimating μ_a by up to ~ +150%/-40% produced D_B percentage errors up to ~ +40%/-20%. Overestimating/underestimating μ_s' by up to ~ +175%/-35% produced D_B percentage errors up to ~ -80%/+110%. The phantom properties chosen for calibration may have influence over the optical properties estimation errors.

4.4 *In-vivo* Tumor Study Data in Comparison to Phantom Study Results

Optical property variations were large between the patients in the head and neck tumor study (see **Fig. 26** and **27**). This scenario proves useful for analyzing real-tissue implications of the phantom study results. The optical properties of patients covered: μ_a (830 nm) from 0.07 to 0.16 cm^{-1} and μ_s' (830 nm) from 5.35 to 13.1 cm^{-1}. These properties are within the same range as those tested in the phantom experiments. The trends in αD_B, resulting from calculations with the different optical property sets, are in agreement with conclusions from the phantom study. Overestimating/underestimating the μ_a and μ_s' (using maximum and minimum) produce underestimation/overestimation of the DCS flow index (αD_{B-max} and αD_{B-min}). Thus, the variations in μ_s' appear to be the greater factor in influencing αD_B errors than that of μ_a. Depending on the optical properties assumed, the errors in αD_B ranged from ~ -70% up to ~ +280%. Comparisons are also made between the estimated αD_B (αD_{B-min}, αD_{B-mean}, and αD_{B-max}) trends and the

true ($\alpha D_{B\text{-dynamic}}$). It is apparent that inaccurate optical property assumptions will alter the patient order based on increasing αD_B and potentially any subsequent conclusions made from this data. Invalid conclusions in similar studies may result from this lack of consideration into optical property influences on DCS flow indices.

4.5 Conclusions

DCS technology has provided deep tissue blood flow measurements in an increasing field of applications thanks to its noninvasive nature and fast data acquisition capabilities. Increasing in concert with these developments are the necessities of ensuring the proper operation and application of the technology. This includes investigating errors that are potentially encountered in measurements, notably the assumption of constant optical properties, μ_a and μ_s'. DCS measurements are described by the extension of light scattering techniques into the diffusive regime of deep tissue, resulting in a correlation diffusion equation. DCS blood flow indices stem from a solution to this equation which includes the parameters of tissue μ_a and μ_s'. With the advent of a hybrid optical instrument developed by our lab, we can now measure tissue optical properties and blood flow simultaneously. By also incorporating liquid phantom creation techniques to control simulated tissue optical properties and flow, investigation of optical property influences on DCS flow indices is now possible. The Brownian diffusion coefficient produced by the Einstein-Stokes formula for particles in liquid was found applicable and usable as the true flow index in comparison to DCS flow indices. The particle motions in the liquid phantoms were determined to be independent of variations in the optical properties. Although inaccurate estimations of both μ_a and μ_s' produced errors in DCS flow indices

55

larger than that when using true values, μ_s' was found to have a more substantial influence. This influence was not identified as being dependent on wavelengths employed. Therefore, the concurrent measurement of tissue optical properties and DCS flow indices is required within studies encountering significant μ_a and μ_s' variations to accurately determine tissue blood flow. The examination of a head and neck tumor study elucidate the possible consequences of ignoring the optical property variations in real tissue measurements.

CHAPTER 5: SUMMARY AND PERSPECTIVES

In summary of this research study, I have provided a quantified generalization of the influences of inaccurate estimations in optical properties on diffuse correlation spectroscopy blood flow measurements by means of liquid phantoms and *in-vivo* analysis. The recent integration by our lab of the Imagent and dual-wavelength DCS flow-oximeter into a hybrid instrument has enabled the ability to carry out this investigation. The design and completion of this study included my contributions to several facets of operation. These contributions consist of the unique phantom study experimental design (Chapter 2.6), determination of ideal hybrid instrument setup (Chapter 2.1 – 2.3), details of liquid phantom composition, measurement equipment and facilitation into our lab (Chapter 2.5), incorporation of measurement errors utilizing Brownian motion and theoretical predictions (Chapter 2.4), exemplification of generalized DCS flow errors through real tissue tumor study analysis (Chapter 2.8), and general methods of data analysis (Chapter 2.7). The results of this study have also been peer reviewed and published [64].

The experimental design of this phantom study was found capable of adequately evaluating the influences of the optical properties on DCS flow indices. The approach taken in this study sought to minimize variations other than the optical properties. The usage of our hybrid instrument performed as expected without requiring complex modifications or alterations. This was an important facet as this instrument is a means of avoidance into the errors posed by inaccurate optical property estimations. To further this study, an alternative approach would be to analyze Eq. 1 and 3 and determine the

influences of optical property variations with varying parameters, which may be the subject of future work. However, it is expected that without the knowledge of tissue optical properties such extensive quantification may not provide useful results.

The optimal hybrid instrument setup was determined from the following factors. It is expected that DCS flow indices obtained at different wavelengths provide equivalent flow information. To evaluate this aspect, 785 and 830 nm wavelengths were used. Originally, a long coherence length CW NIRS 690 nm laser was attempted instead of 785 nm, but due to technical circumstances was unavailable for this study. Utilizing different laser source wavelengths for both Imagent and DCS may extend the applicability of the results since no wavelengths at the low end of the NIR range were successfully incorporated (i.e., ~650 nm). The next factor of interest is maintaining an optimal SNR for both the Imagent and DCS equipment. The gain for the Imagent PMT was set at as high as possible (without saturation) from the initial phantoms and was not adjusted during each experiment. The source-detector separations and fiber orientation of the Imagent probe were fixed and not deemed necessary for modification. For the DCS system, the detector fibers were bundled and set at an equivalent source-detector separation of 1.5 cm. This distance was chosen due to its compliance with diffusion theory and adequate SNR. The SNR was increased through the averaging of the signal from the four detectors. The range of optical properties chosen also may affect the SNR and will be described shortly. The correlation time of DCS was found to be adequate in detecting the motion of Intralipid particles during both μ_a and μ_s' variations. The Imagent averaged 10 data acquisitions per one frame and DCS about 25 per frame (at both

wavelengths). These averaging parameters were determined to provide sufficiently stable measurements from the hybrid instrument.

There are several options currently available for creating tissue-like phantoms for NIR optical experimentation. Liquid phantoms were chosen over solid phantoms as they are typically easier to create and manipulate. In addition, there is no inherent flow in solid phantoms which would require additional design considerations. The liquid phantoms comprised of Intralipid, distilled water, and India ink proved capable of our needs thanks to their simplicity and versatility. For future studies, modifications to the liquid phantom flow can be induced using methyl cellulose or glycerin to evaluate optical property influences at different absolute DCS flow indices. However, the addition of these elements may have the undesirable effect of also altering the phantom viscosity and optical properties. The constituents were readily accessible without significant overhead and cost with Intralipid requiring the most effort to obtain. To maintain adequate SNR, the optical property ranges in this study were limited. More expansive ranges were tested but produced unreliable and unstable results. In the future, creating liquid phantoms with a broader range of μ_a and μ_s' can test the expansion of current conclusions to a greater variety of tissue types. The container size (aquarium) was chosen for adequate distance from the probe to the sides such that small variations in position did not result in interference due to boundaries. The custom probe holder was designed and put into a schematic prior to machining by the University of Kentucky machine shop. It was designed to be incorporated with the lab stand available providing stability and axial and longitudinal positioning.

Measurement errors for the DCS and Imagent were determined based on previous studies to differentiate actual optical property influences on DCS flow indices and those resulting from other factors. This includes the liquid phantom preparations and measurement variations. The methods for expected value predictions were advantageous in that they have already been discussed and used elsewhere allowing for quick implementation into our experimental design. Brownian motion for spherical particles in liquid is used for comparison with DCS. Spectrometer and Mie theory are used for comparison with the Imagent measurements. The measurements of viscosity and temperature related to Brownian motion required testing several apparatus setups. For viscosity, a spindle viscometer was tested but had inadequate range due to the low viscosity of distilled water, India ink, and Intralipid solutions. A cone-plate viscometer with better low viscosity accuracy was purchased and performed adequately. No continuous viscosity data could be acquired due to the induced motion of pumping liquid phantom solution through the viscometer. The current study employs all solutions and liquid phantoms at ambient temperature. This method provided the most stable temperature over other methods such as immersing the aquarium into a larger water filled container temperature controlled by an immersion circulator. More than one spectrometer was tested in the determination of the India ink absorption coefficient: a 96-well plate reader (Biotek), Jaz (Ocean Optics), and the Beckman Coulter as reported. Results were comparable between the three, but the Beckman Coulter device was chosen due to availability and speed of usage.

The tumor study required analyzing the hybrid equipment already in usage for that study and reasonably comparing it to the phantom study. There is inherently greater

difficulty and complexity involved in *in-vivo* tissue optical property and flow measurements. Multiple DCS source-detector separations and wavelengths were used for the head and neck tumor measurements. To properly attribute the optical property influences on DCS flow indices the depth chosen was matched as closely as possible to that of the Imagent. Although the tissue is assumed homogeneous for the purposes of the theoretical models used, the best agreement between regions probed by the two systems was chosen. The optical properties of the patients were within the range used in the phantom study and it is expected that these will be similar for other tissue types, but a holistic representation is beyond the scope of this study and should be determined based on the context. More variations in absolute DCS flow indices were expected due to anatomical and other subject differences. The agreement with the phantom study results provides further insight as to the applicability of the generalized results into *in-vivo* measurements.

To facilitate data analysis, a custom Matlab program was written to calculate DCS flow using various sets of optical properties and variations. Only those flows incorporating dynamic and constant property sets were included in this paper. This was done to simplify the analysis and provide a less complex, but more usable realization of the results. Data had to be extracted from the different files produced by the DCS and Imagent for processing. A robust program was written automating data analysis while providing control such as wavelengths used, source detector separations and processing methods (constant vs. dynamic optical properties). The creation of correlation curve figures each frame requires significant hard drive space which should be considered if saving is desirable. The method of analysis using averaged optical properties over the

61

intervals was determined acceptable as exhibited by measurement stability. However, in real tissue measurements, transient fluctuations in optical properties can occur and averaged properties may not be applicable.

REFERENCES

1.	Durduran, T., et al., *Diffuse optical measurement of blood flow in breast tumors.* Opt Lett, 2005. **30**(21): p. 2915-7.
2.	Sunar, U., et al., *Noninvasive diffuse optical measurement of blood flow and blood oxygenation for monitoring radiation therapy in patients with head and neck tumors: a pilot study.* J Biomed Opt, 2006. **11**(6): p. 064021.
3.	Yu, G., et al., *Intraoperative evaluation of revascularization effect on ischemic muscle hemodynamics using near-infrared diffuse optical spectroscopies.* J Biomed Opt, 2011. **16**(2): p. 027004.
4.	Yu, G., et al., *Noninvasive monitoring of murine tumor blood flow during and after photodynamic therapy provides early assessment of therapeutic efficacy.* Clin Cancer Res, 2005. **11**(9): p. 3543-52.
5.	Li, J., et al., *Noninvasive detection of functional brain activity with near-infrared diffusing-wave spectroscopy.* J Biomed Opt, 2005. **10**(4): p. 44002.
6.	Ubbink, D.T., et al., *Skin microcirculation in diabetic and non-diabetic patients at different stages of lower limb ischaemia.* Eur J Vasc Surg, 1993. **7**(6): p. 659-6.
7.	Wahlberg, E., et al., *Level of arterial obstruction in patients with peripheral arterial occlusive disease (PAOD) determined by laser Doppler fluxmetry.* Eur J Vasc Surg, 1993. **7**(6): p. 684-9.
8.	Bonner, R. and R. Nossal, *Model for laser Doppler measurements of blood flow in tissue.* Appl Opt, 1981. **20**: p. 2097-2107.
9.	Wang, R.K. and L. An, *Doppler optical micro-angiography for volumetric imaging of vascular perfusion in vivo.* Opt Express, 2009. **17**(11): p. 8926-40.
10.	Chen, Z., et al., *Optical Doppler tomographic imaging of fluid flow velocity in highly scattering media.* Opt Lett, 1997. **22**(1): p. 64-6.
11.	Li, L., et al., *Three-dimensional combined photoacoustic and optical coherence microscopy for in vivo microcirculation studies.* Opt Express, 2009. **17**(19): p. 16450-5.
12.	Durduran, T., *Non-invasive measurements of tissue hemodynamics with hybrid diffuse optical methods.* 2004, University of Pennsylvania, Dissertation.
13.	Zhou, C., *In-vivo optical imaging and spectroscopy of cerebral hemodynamics.* 2007, University of Pennsylvania, Dissertation.
14.	Boas, D.A., *Diffuse photon probes of structural and dynamical properties of turbid media: Theory and biomedical applications.* 1996, University of Pennsylvania, Dissertation.
15.	Boas, D.A. and A.G. Yodh, *Spatially varying dynamical properties of turbid media probed with diffusing temporal light correlation.* J Opt Soc Am A Opt Image Sci Vis, 1997. **14**(1): p. 192-215.
16.	Xu, R., *Particle Characterization: Light Scattering Methods.* Particle Technology Series, ed. B. Scarlett. 2000, Netherlands: Kluwer Academic Publishers. 397.
17.	Boas, D.A., L.E. Campbell, and A.G. Yodh, *Scattering and imaging with diffusing temporal field correlations.* Phys Rev Lett, 1995. **75**(9): p. 1855-1858.
18.	Cheung, C., et al., *In vivo cerebrovascular measurement combining diffuse near-infrared absorption and correlation spectroscopies.* Phys Med Biol, 2001. **46**(8): p. 2053-2065.

19. Jaillon, F., et al., *Activity of the human visual cortex measured non-invasively by diffusing-wave spectroscopy.* Opt Express, 2007. **15**(11): p. 6643-6650.

20. Buckley, E.M., et al., *Cerebral hemodynamics in preterm infants during positional intervention measured with diffuse correlation spectroscopy and transcranial Doppler ultrasound.* Opt Express, 2009. **17**(15): p. 12571-81.

21. Roche-Labarbe, N., et al., *Noninvasive optical measures of CBV, StO(2), CBF index, and rCMRO(2) in human premature neonates' brains in the first six weeks of life.* Hum Brain Mapp, 2010. **31**(3): p. 341-52.

22. Menon, C., et al., *An integrated approach to measuring tumor oxygen status using human melanoma xenografts as a model.* Cancer Res, 2003. **63**(21): p. 7232-7240.

23. Kim, M.N., et al., *Noninvasive measurement of cerebral blood flow and blood oxygenation using near-infrared and diffuse correlation spectroscopies in critically brain-injured adults.* Neurocrit Care, 2010. **12**(2): p. 173-80.

24. Zhou, C., et al., *Diffuse optical monitoring of hemodynamic changes in piglet brain with closed head injury.* J Biomed Opt, 2009. **14**(3): p. 034015.

25. Durduran, T., et al., *Diffuse optical measurement of blood flow, blood oxygenation, and metabolism in a human brain during sensorimotor cortex activation.* Opt Lett, 2004. **29**(15): p. 1766-8.

26. Culver, J.P., et al., *Diffuse optical tomography of cerebral blood flow, oxygenation, and metabolism in rat during focal ischemia.* J Cereb Blood Flow Metab, 2003. **23**(8): p. 911-924.

27. Li, J., et al., *Transient functional blood flow change in the human brain measured noninvasively by diffusing-wave spectroscopy.* Opt Lett, 2008. **33**(19): p. 2233-5.

28. Zhou, C., et al., *Diffuse optical monitoring of blood flow and oxygenation in human breast cancer during early stages of neoadjuvant chemotherapy.* J Biomed Opt, 2007. **12**(5): p. 051903.

29. Zhou, C., et al., *Diffuse optical correlation tomography of cerebral blood flow during cortical spreading depression in rat brain.* Opt Express, 2006. **14**: p. 1125-1144.

30. Busch, T.M., et al., *Fluence rate-dependent intratumor heterogeneity in physiologic and cytotoxic responses to Photofrin photodynamic therapy.* Photochem Photobiol Sci, 2009. **8**(12): p. 1683-1693.

31. Sunar, U., et al., *Hemodynamic responses to antivascular therapy and ionizing radiation assessed by diffuse optical spectroscopies.* Opt Express, 2007. **15**(23): p. 15507-15516.

32. Yu, G., et al., *Real-time in situ monitoring of human prostate photodynamic therapy with diffuse light.* Photochem Photobiol, 2006. **82**(5): p. 1279-84.

33. Durduran, T., et al., *Optical measurement of cerebral hemodynamics and oxygen metabolism in neonates with congenital heart defects.* J Biomed Opt, 2010. **15**(3): p. 037004.

34. Koban, L., et al., *Processing of emotional words measured simultaneously with steady-state visually evoked potentials and near-infrared diffusing-wave spectroscopy.* BMC Neurosci, 2010. **11**: p. 85.

35. Edlow, B.L., et al., *The effects of healthy aging on cerebral hemodynamic responses to posture change.* Physiol Meas, 2010. **31**(4): p. 477-95.

36. Durduran, T., et al., *Transcranial optical monitoring of cerebrovascular hemodynamics in acute stroke patients.* Opt Express, 2009. **17**(5): p. 3884-902.

37. Shang, Y., et al., *Cerebral monitoring during carotid endarterectomy using near-infrared diffuse optical spectroscopies and electroencephalogram.* Phys Med Biol, 2011. **56** p. 3015-3032.

38. Ninck, M., M. Untenberger, and T. Gisler, *Diffusing-wave spectroscopy with dynamic contrast variation: disentangling the effects of blood flow and extravascular tissue shearing on signals from deep tissue.* Biomed Opt Express, 2010. **1**(5): p. 1502-1513.

39. Belau, M., et al., *Noninvasive observation of skeletal muscle contraction using near-infrared time-resolved reflectance and diffusing-wave spectroscopy.* J Biomed Opt, 2010. **15**(5): p. 057007.

40. Shang, Y., et al., *Effects of muscle fiber motion on diffuse correlation spectroscopy blood flow measurements during exercise.* Biomed Opt Express, 2010. **1**(2): p. 500-511.

41. Yu, G., et al., *Validation of diffuse correlation spectroscopy for muscle blood flow with concurrent arterial spin labeled perfusion MRI.* Opt Express, 2007. **15**(3): p. 1064-1075

42. Dietsche, G., et al., *Fiber-based multispeckle detection for time-resolved diffusing-wave spectroscopy: characterization and application to blood flow detection in deep tissue.* Appl Opt, 2007. **46**(35): p. 8506-14.

43. Yu, G., et al., *Time-dependent blood flow and oxygenation in human skeletal muscles measured with noninvasive near-infrared diffuse optical spectroscopies.* J Biomed Opt, 2005. **10**(2): p. 024027.

44. Shang, Y., et al., *Portable optical tissue flow oximeter based on diffuse correlation spectroscopy.* Opt Lett, 2009. **34**(22): p. 3556-8.

45. Mesquita, R.C., et al., *Hemodynamic and metabolic diffuse optical monitoring in a mouse model of hindlimb ischemia.* Biomed Opt Express, 2010. **1**(4): p. 1173-1187.

46. Peskir, G., *On the diffusion coefficient: The Einstein relation and beyond.* Stoch Models, 2003. **19**(3): p. 383-405.

47. Wallace, D., et al. *Summary of the results of a 95 subject human clinical trial for the diagnosis of peripheral vascular disease using a near infrared frequency domain hemoglobin spectrometer.* in *Proc. of SPIE.* 1999.

48. Fantini, S., M.A. Franceschini, and E. Gratton, *Semi-infinite-geometry boundary-problem for light migration in highly scattering media - a frequency-domain study in the diffusion-approximation.* J Opt Soc Am B, 1994. **11**(10): p. 2128-2138.

49. Jaillon, F., et al., *Diffusing-wave spectroscopy from head-like tissue phantoms: influence of a non-scattering layer.* Opt Express, 2006. **14**(22): p. 10181-94.

50. Culver, J.P., et al., *Three-dimensional diffuse optical tomography in the parallel plane transmission geometry: Evaluation of a hybrid frequency domain/continuous wave clinical system for breast imaging.* Med Phys, 2003. **30**(2): p. 235-247.

51. Boas, D.A., et al., *Three dimensional Monte Carlo code for photon migration through complex heterogeneous media including the adult human head.* Opt Express, 2002. **10**(3): p. 159-170.

52. Gagnon, L., et al., *Investigation of diffuse correlation spectroscopy in multi-layered media including the human head.* Opt Express, 2008. **16**(20): p. 15514-30.

53. Kim, J.G. and H. Liu, *Investigation of biphasic tumor oxygen dynamics induced by hyperoxic gas intervention: the dynamic phantom approach.* Appl Opt, 2008. **47**(2): p. 242-52.

54. Rice, S.O., *Mathematical analysis of random noise*, in *Noise and Stochastic Processes*, N. Wax, Editor. 1954, Dover: New York. p. 133.

55. Walker, S.A., S. Fantini, and E. Gratton. *Effect of index of refraction mismatch on the recovery of optical properties of cylindrical inhomogeneities in an infinite turbid medium.* in *Proc. of SPIE*. 1997.

56. Li, X., *Fluorescence and diffusive wave diffraction tomographic probes in turbid media*. 1998, University of Pennsylvania, Dissertation.

57. Hueber, D., et al. *New optical probe designs for absolute (self-calibrating) NIR tissue hemoglobin measurements*. in *Proc. of SPIE*. 1999.

58. EngineeringToolBox. *Unit Converter with the most Common Units*. Available from: http://www.engineeringtoolbox.com/unit-converter-d_185.html.

59. Choe, R., *Diffuse optical tomography and spectroscopy of breast cancer and fetal brain*. 2005, University of Pennsylvania, Dissertation.

60. Prahl, S.A. *Optical properties spectra*. Available from: http://omlc.ogi.edu/spectra/index.html.

61. van Staveren, H.J., et al., *Light scattering in Intralipid-10% in the wavelength range of 400-1100 nm.* Appl Opt, 1991. **30**: p. 4507-4514.

62. Fantini, S., et al., *Quantitative determination of the absorption spectra of chromophores in strongly scattering media: a light-emitting-diode based technique.* Appl Opt, 1994. **33**(22): p. 5204-13.

63. Spichtig, S., et al., *Multifrequency frequency-domain spectrometer for tissue analysis.* Rev Sci Instrum, 2009. **80**(2): p. 024301.

64. Irwin, D., et al., *Influences of tissue absorption and scattering on diffuse correlation spectroscopy blood flow measurements.* Biomed Opt Express, 2011. **2**(7): p. 1969-1985.

VITA

DATE & PLACE OF BIRTH
    June 15, 1980 in Louisville, KY

EDUCATION
    University of Louisville, Louisville, KY
    Bachelor of Science in Computer Engineering
        and Computer Science   2008

PROFESSIONAL POSITIONS
    University of Kentucky Center for Biomedical Engineering
    Biophotonics Laboratory
    Lexington, KY
    Research Assistant   2009 – Present

SCHOLASTICS & PROFESSIONAL HONORS
    Student Travel Support, University of Kentucky   2011

PUBLICATIONS

D. Irwin, L. Dong, Y. Shang, R. Cheng, M. Kudrimoti, S. D. Stevens, and G. Yu, *Influences of tissue absorption and scattering on diffuse correlation spectroscopy blood flow measurements.* Biomed Opt Express, 2011. **2**(7): p. 1969-1985.

Y. Shang, Y. Zhao, R. Cheng, L. Dong, D. Irwin, and G. Yu, *Portable optical tissue flow oximeter based on diffuse correlation spectroscopy.* Opt Lett, 2009. **34**(22): p. 3556-8.

PRESENTATIONS/ABSTRACTS in CONFERENCES/PROCEEDINGS

D. Irwin, L. Dong, Y. Shang, R. Cheng, M. Kudrimoti, S. D. Stevens, and G. Yu, "*Influences of tissue absorption and scattering on diffuse correlation spectroscopy blood flow measurements in head and neck tumors*", in 2011 Advances in Optics for Biotechnology, Medicine and Surgery XII, ECI Conferences, Naples, FL, USA (2011)

D. Irwin, L. Dong, Y. Shang, R. Cheng, M. Kudrimoti, S. D. Stevens, and G. Yu, "*Influences of tissue absorption and scattering on diffuse correlation spectroscopy blood flow measurements in head and neck tumors*", in 2011 Markey Cancer Center Research Day, University of Kentucky (2011)

Y. Shang, R. Cheng, L. Dong, D. Irwin, K. M. Gurley, K. R. Swartz, S. S. Salles, and G. Yu, "*Evaluation of electronic stimulation impact on muscle hemodynamics using diffuse optical spectroscopies*", 23rd Annual Physical Medicine and Rehabilitation Research Day, Lexington, KY, USA (2011)

Y. Shang, Y. Zhao, R. Cheng, L. Dong, <u>D. Irwin</u>, K. R. Swartz, S. S. Salles, and G. Yu, "*Diffuse optical spectroscopies for evaluation of muscle hemodynamic enhancements by electrical stimulation*", in 2010 Biomedical Optics and 3-D Imaging, OSA Optics & Photonics Congress, Miami, FL, USA (2010)

Y. Shang, Y. Zhao, R. Cheng, L. Dong, <u>D. Irwin</u>, K. R. Swartz, S. S. Salles, and G. Yu, "*Diffuse optical spectroscopies for evaluation of muscle hemodynamic enhancements by electrical stimulation*", UK Muscle Biology Fall Retreat, Lexington, KY, USA (2010)

G. Yu, Y. Shang, Y. Zhao, R. Cheng, L. Dong, <u>D. Irwin</u>, and S. P. Saha, "*Portable optical tissue flow oximeter for evaluation of revascularization effect on ischemic muscle hemodynamics*", in 2010 Biomedical Optics and 3-D Imaging, OSA Optics & Photonics Congress, Miami, FL, USA (2010)

G. Yu, Y. Zhao, R. Cheng, L. Dong, and <u>D. Irwin</u>, "*A portable optical tissue flow-oximeter based on diffuse correlation spectroscopy*", in BiOS SPIE Photonics West. San Francisco, CA, USA (2010)

Y. Shang, Y. Zhao, R. Cheng, <u>D. Irwin</u>, L. Dong, K. R. Swartz, S. S. Salles, and G. Yu, "*Noninvasive assessment of muscle hemodynamic enhancement by electrical stimulation using diffuse optical spectroscopies*", Fall Annual Meeting of the Biomedical Engineering Society, Pittsburgh, PA, USA (2009)

G. Yu, Y. Shang, Y. Zhao, R. Cheng, <u>D. Irwin</u>, L. Dong, K. R. Swartz, and S. S. Salles, "*Diffuse optical evaluation of muscle hemodynamic responses to electrical stimulation*", 2nd Photonics and OptoElectronics Meetings (POEM 2009), Wuhan, China (2009)

Y. Shang, Y. Zhao, R. Cheng, <u>D. Irwin</u>, L. Dong, K. R. Swartz, S. S. Salles, and G. Yu, "*Noninvasive assessment of muscle hemodynamic enhancement by electrical stimulation using diffuse optical spectroscopies*", Adult Skeletal Muscle Symposium: Clinical Problems, Molecular Targets, University of Kentucky (2009)

Y. Shang, Y. Zhao, R. Cheng, <u>D. Irwin</u>, L. Dong, K. R. Swartz, S. S. Salles, and G. Yu, "*Noninvasive assessment of muscle hemodynamic enhancement by electrical stimulation using diffuse optical spectroscopies*", UK Linda and Jack Gill Heart Institute Cardiovascular Research Day, University of Kentucky (2009)

TYPED NAME
_____

Daniel A. Irwin